Evolution of circular, non-equatorial orbits of Kerr black holes due to gravitational-wave emission: II. Inspiral trajectories and gravitational waveforms

Scott A. Hughes
Institute for Theoretical Physics, University of California, Santa Barbara, CA 93103
Theoretical Astrophysics, California Institute of Technology, Pasadena, CA 91125

The inspiral of a "small" ($\mu \sim 1 - 100\,M_\odot$) compact body into a "large" ($M \sim 10^{5-7}\,M_\odot$) black hole is a key source of gravitational radiation for the space-based gravitational-wave observatory LISA. The waves from such inspirals will probe the extreme strong-field nature of the Kerr metric. In this paper, I investigate the properties of a restricted family of such inspirals (the inspiral of circular, inclined orbits) with an eye toward understanding observable properties of the gravitational waves that they generate. Using results previously presented to calculate the effects of radiation reaction, I assemble the inspiral trajectories (assuming that radiation reacts adiabatically, so that over short timescales the trajectory is approximately geodesic) and calculate the wave generated as the compact body spirals in. I do this analysis for several black hole spins, sampling a range that should be indicative of what spins we will encounter in nature. The spin has a very strong impact on the waveform. In particular, when the hole rotates very rapidly, tidal coupling between the inspiraling body and the event horizon has a very strong influence on the inspiral time scale, which in turn has a big impact on the gravitational wave phasing. The gravitational waves themselves are very usefully described as "multi-voice chirps": the wave is a sum of "voices", each corresponding to a different harmonic of the fundamental orbital frequencies. Each voice has a rather simple phase evolution. Searching for extreme mass ratio inspirals voice-by-voice may be more effective than searching for the summed waveform all at once.

PACS numbers: 04.30.Db, 04.30.-w, 04.25.Nx, 95.30.Sf

I. INTRODUCTION

A. Motivation: extreme mass ratio inspirals

One of the goals of the space-based gravitational-wave detector LISA [1] is to make measurements that will probe gravity in the very strong field. The most stringent probes will involve binary black hole systems. Mergers of comparable mass black holes will be detectable throughout most of the universe [2]; their measurements will probe the violent dynamics of the two black holes combining to form a single hole. LISA will measure hundreds to thousands of wave cycles in such events, probing their waveforms with moderate precision. When the mass ratio of the system is extreme ($M_1/M_2 \simeq 10^{-3} - 10^{-7}$), measurement of the waves probes the quiescent structure of the Kerr black hole spacetime. LISA should measure tens of thousands to millions of cycles from such inspirals (depending mostly on mass ratio), and thus may be able to measure their waves — and probe black hole spacetimes — with extremely high precision. Extreme mass ratio inspirals will be the focus of this analysis.

Extreme mass ratio inspirals occur when a compact body is scattered, through multi-body interactions, from the cluster at the core of a galaxy into a tightly bound orbit of the central black hole. How often such events occur is somewhat uncertain. The mass range of large black holes relevant to LISA is roughly $10^5\,M_\odot \lesssim M \lesssim 10^7\,M_\odot$ — if the holes are larger, the wave frequencies are too low to be of interest; smaller holes are not thought to be abundant enough to be interesting. Estimates that fold the presumed abundance of the relevant black holes into dynamical models for the behavior of stars in the central galactic cluster suggest that, out to about 1 Gigaparsec, extreme mass ratio inspirals occur at a rate of 1/year to 1/month [3,4]. Reference [3] emphasizes that the lower limit of 1/year assumes extremely conservative bounds on the distribution of black hole masses and galactic central densities. A multi-year LISA mission is likely to see at least several extreme mass ratio inspirals.

The orbit of the compact body will initially be extremely eccentric ($e = 1 - \epsilon$, where $\epsilon \ll 1$ [5]), but will rapidly become more circular due to gravitational-wave emission. When the orbit has shrunk enough that all of the system's orbital periods enter the LISA frequency band[1], $0.1 \lesssim e \lesssim 0.9$ [6]. The small body then spends roughly a year

[1]Before the eccentricity has shrunk this much, the waves emitted at peribothron will be in LISA's band. The (potentially

spiraling in, finally plunging into the hole when it encounters the dynamical instability at the last stable orbit (LSO).

During this year, the body orbits the hole roughly 10^5 times, emitting about the same number of gravitational-wave cycles. Accurately tracking the evolution of the waveform phase over these cycles could make possible extraordinarily precise measurements of the spacetime's characteristics. Fintan Ryan [8] has shown that the waves emitted in this year can be used to reconstruct the multipolar structure of the black hole, measuring the detailed structure of the Kerr metric. Because a black hole has only two independent multipole moments (the mass M and spin a), measurement of more than two moments could be used to test the "no hair" theorem for black holes, or to probe for the existence of more exotic massive objects in galactic cores, such as soliton stars. It is worth noting here that accreting material in galactic cores is unlikely to significantly influence the gravitational waveform in most cases. Narayan [9] has shown that accretion profiles appropriate for active galaxies strongly impact the orbit's evolution and hence the gravitational waves that are generated, but that advection dominated accretion flows (ADAF) more appropriate to "normal" galaxies have negligible impact. Updates of the ADAF model, such as convection dominated accretion flows (CDAF) [10], have even less impact on inspiral, since the density of gas close to the black hole is even smaller [9,11]. Inspiral into the vast majority of massive black holes in the universe depends only on the structure of spacetime, not on the nature of accreting matter.

Ryan's analysis suggests that, for many measured inspirals, LISA is likely to be able to measure at least three and perhaps four or five of the massive body's multipole moments (depending quite a bit on the mass and mass ratio of the system). However, his analysis is rather specialized: he assumes, for simplicity, that the orbit is circular and confined to the large body's equatorial plane. This is quite unrealistic. From the discussion above, we expect extreme mass ratio binaries to have some non-negligible eccentricity. From the nearly spherical symmetry of galaxies' central density cusps, the binaries should have essentially random inclination. A realistic analysis of LISA's prospects for measuring the multipole moments of massive bodies must examine gravitational waves from eccentric, inclined orbits of bodies with arbitrary multipole moments. Indeed, one would expect that the accuracy with which one can determine the various multipole moments will improve as the orbits are made more generic — there are more "handles" with which one can probe the central body's structure.

In the weak field, one can build the spacetime of body with arbitrary multipoles moments using the formalism of of Fodor, Hoenselaers and Perjés [12]. The massive body's multipole moments affect the spacetime via the Ernst potential [13]. One can then study the orbits and radiation generation/propagation in this spacetime as a foundation for studies of gravitational-wave measurement. (This is in fact how Ryan sets up his analysis; cf. Ref. [14].) A different approach must be used in the strong field, but no matter of principle stands in the way of doing so.

Such an analysis is rather daunting. The generic orbits of bodies with arbitrary multipole moments will not possess the same integrals of the motion as a Kerr black hole: stationarity and axisymmetry guarantee that orbits will have well-defined energy E and axial angular momentum L_z, but there is unlikely to be an analog of the Kerr metric's Carter constant Q (whose existence is something of a miracle of the Kerr geometry). A description of the small body's motion in this spacetime is thus likely to be somewhat complicated. The generation and propagation of gravitational radiation generated by these orbits is also likely to be difficult to study. When the central body is a Kerr black hole, the wave equation for all radiation fields separates [15], allowing many useful techniques to be applied which make solving the radiation comparatively simple (see, *e.g.*, Ref. [16] and references therein). This won't be the case in general; wave generation and propagation will need to be analyzed using a complicated partial differential equation.

An additional complication is that the inspiraling body undoubtably will be spinning itself. The spin of this body will couple to the large body's curvature [17], forcing its motion to be non-geodesic. Janna Levin has shown [18,19] that in the comparable mass ratio case this coupling can lead to chaotic orbital development. It is not clear if this is the case in the extreme mass mass ratio — the smaller mass ratio tends to suppress the effects of the coupling, but the larger number of cycles may counteract this suppression. Work in progress [20] will hopefully clarify this soon.

We are far from being able to understand the gravitational-wave driven inspiral of spinning compact objects into massive bodies with arbitary multipole moments. As a foundation for understanding the kinds of waves that LISA can expect to measure, the focus of this paper will be rather restricted: the inspiraling body will be non-spinning so that the motion is geodesic (modulo radiation reaction), and the massive object will be a Kerr black hole.

---

many) extreme mass ratio systems that still have substantial eccentricity and are not close to merger may thus constitute an important source of waves. I thank Sterl Phinney for pointing this out to me.

B. Radiation reaction on geodesic Kerr orbits

Having restricted the class of systems that will be analyzed, one might guess that analyzing their evolution is now straightforward: the motion is approximated as a geodesic of the background spacetime $g^{\rm Kerr}_{\alpha\beta}$, augmented by radiative corrections. Since the orbiting body is taken to be much less massive than the hole, the magnitude of the spacetime corrections $h_{\alpha\beta}$ due to that body will be much smaller than the typical components of $g^{\rm Kerr}_{\alpha\beta}$:

$$\frac{||h_{\alpha\beta}||}{||g^{\rm Kerr}_{\alpha\beta}||} \sim \frac{\mu}{M} \ , \tag{1.1}$$

where M is the mass of the black hole and μ is the mass of the orbiting body. Radiative effects can thus be analyzed using perturbation theory [at least up to corrections of order $(\mu/M)^2$]. In particular, consider the particle's worldline to be geodesic plus the influence of a "radiation reaction force" $f^\alpha_{\rm RR}$ that pushes the motion off of the geodesic:

$$\frac{dx^\alpha}{d\tau} = \left.\frac{dx^\alpha}{d\tau}\right|_{\rm geodesic} + \int d\tau\, f^\alpha_{\rm RR} \ , \tag{1.2}$$

where τ is proper time measured along the small body's geodesic. For the purposes of this paper, $f^\alpha_{\rm RR}$ encapsulates the manner in which radiation emission changes the orbit's properties and drives the small body to spiral in [21].

Programs to compute this force are currently underway in several groups, using various approaches. A prescription for computing $f^\alpha_{\rm RR}$ has been developed independently by Mino *et al.* [22] and by Quinn and Wald [23]. Implementations (particularly for the most interesting case of gravitational interactions, as opposed to scalar or electromagnetic interactions) are in a somewhat early state [24–32]. Although maturing, it is unlikely that these implementations will have much to say about astrophysical extreme mass ratio binaries in the near term. Another method must be used to calculate the radiative effects.

Suppose the inspiral is adiabatic — the timescale $T_{\rm RR}$ for radiation reaction to change the orbit is much greater than the orbital timescale $T_{\rm orb}$. Then, over timescales of order $T_{\rm orb}$, the small body's worldline is indistinguishable from a geodesic orbit of the black hole. Adiabatic radiation reaction can be understood as the slow evolution of the "conserved" constants of Kerr orbits (energy E, axial angular momentum L_z, and Carter constant Q). One can consider (E, L_z, Q) to be coordinates in the phase space of allowed orbits. Radiation emission evolves these constants and thus traces out a trajectory in this orbital phase space — the inspiraling body moves through a sequence of geodesic orbits.

A well-developed technique [33–37] for extracting the changes in the orbit's conserved quantities uses the Teukolsky equation [15] to compute the gravitational-wave flux to infinity and into the black hole. This flux carries energy and angular momentum, so it is straightforward to extract $\dot{E}$ and $\dot{L}_z$ and evolve those orbital constants. It is not straightforward to extract the change in Q, however — to date, this is an unsolved problem. When the large black hole is Schwarzschild, $Q = L_x^2 + L_y^2$. In this case, $\dot{Q} = 2(L_x\dot{L}_x + L_y\dot{L}_y)$, which can be pulled from the gravitational-wave flux. When $a \neq 0$, Q is not simply related to L_x and L_y (the geometry becomes oblate, and frame dragging entangles the timelike and axial coordinates). No method has been found in this case to relate $\dot{Q}$ to quantities that are directly extractable from the wave flux.

The inability to evolve the Carter constant forces us to consider restricted problems in which we can infer Q's evolution. One particularly simple case is the evolution of equatorial orbits — they have $Q = 0$ and remain in the plane, so $\dot{Q} = 0$. An analysis of radiation reaction on such orbits about Kerr black holes should appear very soon [38]. Another simple case is the evolution of "circular" orbits — orbits that have constant Boyer-Lindquist radius, but are inclined out of the equatorial plane. Such orbits belong to a two parameter subset of the bound Kerr orbits, so the value of Q for an orbit is fully determined by knowledge of E and L_z. It has been shown that, under adiabatic radiation reaction, circular orbits remain circular — they do not become eccentric, but change only their radius and inclination angle [39–41]. This "circular goes to circular" rule constrains the orbital evolution such that one can write down a relation for $\dot{Q}$ as a function $\dot{E}$ and $\dot{L}_z$.

Circular orbits will be the focus of this analysis. A previous paper [37] showed how to compute $\dot{E}$, $\dot{L}_z$, and $\dot{Q}$ from radiation emitted by circular orbits using the Teukolsky equation, and how the orbital radius r and inclination angle ι change as a consequence. This paper uses the techniques of Ref. [37] to compute the circular trajectory that a small body would follow as it spirals into a Kerr black hole, as well as the gravitational waveforms emitted as it falls in. Because of the restriction to circular orbits, these results are quite unlikely to be directly applicable to astrophysical extreme mass ratio inspirals. However, the techniques developed here should be applicable to more generic inspirals (when radiation reaction formalisms have matured enough that they can evolve the astrophysically interesting cases), and it is likely that observationally interesting features in these restricted inspirals will be present (with some modifications) in the general case.

C. Summary of this paper

This paper begins by reviewing the properties of circular, inclined orbits of Kerr black holes, and of the radiation reaction formalism that is used here. This material is presented in far greater detail in Refs. [37] and [42]. Here, I simply review the key equations and point the reader to the relevant literature for a detailed derivation.

As discussed above, circular, inclined Kerr orbits are a subset of the Kerr geodesics. The Carter constant Q of these orbits is set by the energy E and axial angular momentum L_z; up to initial conditions, this fully specifies a particular orbit. These constants are conveniently remapped to an orbital radius r and an inclination angle ι. In Sec. II A, I describe how to solve the Kerr geodesic equations to find allowed circular orbits. I have found it convenient in most cases to parameterize these orbits by their radius and the orbital energy; it is simple to find the energy for the most- and least-strongly bound orbits, and then to map out all allowed orbits between these extremes. I summarize formulas which allow one to find the constants L_z and Q as a function of r and E. The orbits themselves are biperiodic with fundamental frequencies Ω_ϕ (related to the rate at which an orbit circles the hole's spin axis) and Ω_θ (related to the rate at which it oscillates through its full range of motion in θ). I summarize closed-form expressions for these two frequencies (in terms of elliptic integrals), good for arbitrary spin and orbital inclination.

In the limit of adiabatic radiation reaction, gravitational-wave backreaction is manifested as a slow change to (E, L_z, Q). I describe how the gravitational-wave flux may be deduced from solutions to the Teukolsky equation in Sec. II B, and how to extract the change in E and L_z from that flux. The fact that circular orbits cannot become eccentric provides a constraint which sets the rate of change of Q as a function of the rates of change of E and L_z. The radiation reaction information is then conveniently summarized as the direction $(\dot{r}, \dot{\iota})$ in which gravitational-wave emission tends to drive the orbit, and as a set of complex amplitudes Z^H_{lmk} which constitute a multipole expansion of the gravitational-wave strain measured by distant observers. This fully sets up the problem considered here, and provides us with enough information to begin studying inspirals.

To actually make an inspiral trajectory — the curve $[r(t), \iota(t)]$ followed by a small body — I use the radiation reaction data $(\dot{r}, \dot{\iota})$ to perform Euler method integrations. Inspiral starts at some coordinate (r_0, ι_0), and advances to $(r_0 + \dot{r}\delta t, \iota_0 + \dot{\iota}\delta t)$ for some chosen step size δt. Steps repeat until the body hits the last dynamically stable orbit and plunges into the hole. Because computing the data $(\dot{r}, \dot{\iota})$ is quite computationally expensive, I actually compute these data on a grid that covers the parameter space of allowed orbits deep in the strong field and use interpolation to get radiative effects at parameter space coordinates off the grid. Details of how this is done are described in Sec. III. Section III A first describes how the data grid is set up, as well as which data are stored on it. For example, $\dot{r}$ turns out to be a very poor choice to store on the grid because it diverges as the dynamical instability is approached. Instead, the quantity $(\cos\iota - \cos\iota_{\rm LSO})\dot{r}$ is stored (where $\iota_{\rm LSO}$ is the radius-dependent inclination angle of the last stable orbit). This prefactor very nicely clears away the divergence, leading to data which interpolate very smoothly. Section III B then briefly describes how the integration is done.

Results of this analysis are presented in Secs. IV and V. First I discuss the inspiral trajectories in Sec. IV; they and their various features are displayed for several choices of black hole spin in Figs. 2, 3, 6, 7, and 8. The trajectories show that during inspiral lasting 1–2 years, the inspiraling body executes several hundred thousand orbits and spirals through the extreme strong field of the massive black hole. This is not a surprise, and has of course been known for quite some time. More interesting is that the inclination angle barely changes during inspiral, particularly when the Kerr spin parameter $a \lesssim 0.8M$. This suggests that it would be worthwhile to explore "faking" the inspiral of generic Kerr orbits by holding the inclination angle fixed. Setting $\iota =$ constant provides a constraint that would fix the rate of change of the Carter constant provided the changes in E and L_z were known. Somewhat more surprising[2] is that the influence of the black hole's event horizon is very strong. As is described in Sec. IV, the inspiraling body tidally distorts the black hole, causing the event horizon to bulge. This bulge then exerts a torque back on the body. If the hole is rapidly rotating, this torque tends to significantly slow the inspiral, transferring some of the hole's rotational kinetic energy to the orbital motion. Inspiral can be prolonged for several weeks ($\sim 5\%$ of the total inspiral time) by this effect, adding tens of thousands of additional orbits. By contrast, if the hole is rotating slowly, the torque exerted by the horizon bulge speeds up the inspiral. This fascinating coupling of the horizon to the inspiraling body's dynamics is an example of how strong-field features of the Kerr spacetime can be seen in the emitted gravitational waves.

Section V discusses the gravitational waves that are produced as the body spirals inward. It should be strongly emphasized at this point that accurately computing the waveforms is more difficult than computing the inspiral trajectories. The waveforms require computing both the magnitude and phase of the complex waveform amplitudes

[2] At least to this author!

Z^H_{lmk} to high precision; the trajectories can be had with just the magnitude alone. As such, the results shown in Sec. V should be taken as an important first step in generating extreme mass ratio inspiral waves, but can — and should! — be improved dramatically.

Multiple harmonics of the orbital frequencies Ω_ϕ and Ω_θ are very important; cf. Fig. 9. Following a suggestion of Sam Finn, I write the gravitational waveform as a sum over many "voices": $h(t) = \sum h_{lmk}(t)$. Each voice $h_{lmk}(t)$ corresponds to a particular harmonic of the orbital frequencies, and has its own amplitude and phase evolution. Writing the waveform in this manner emphasizes that the phase evolution of *each voice* is rather simple, though the sum may be complicated and difficult to follow. It is likely that this multi-voice structure will carry over to the generic case, simply adding an additional index (corresponding to harmonics of the radial frequency Ω_r). The analysis of LISA data may be facilitated by searching for extreme mass ratio inspirals voice-by-voice, rather than searching for the "chorus" of all voices at the same time.

I conclude in Sec. VI. Besides expanding on the points mentioned here, I suggest directions for future work on this problem. The techniques describe here should be combined with work currently in progress on eccentric, equatorial orbits to develop the inspiral trajectories through the parameter space (r, e) of those orbits, as well as the corresponding inspiral waveforms. In addition, it would be extremely useful to use approximate radiation reaction relations (such as holding the inclination angle fixed) in order to develop inspiral trajectories and waveforms for generic Kerr orbits. With such natural extensions of this analysis, we will move significantly forward in understanding how to map the spacetime of black holes with gravitational-wave observations.

Throughout this paper, an overdot denotes d/dt, and a prime denotes $\partial/\partial r$. An overbar indicates complex conjugation. The quantities t, r, θ, and ϕ refer to the Boyer-Lindquist coordinates. I use relativist's units with $G = 1 = c$ throughout.

II. REVIEW: CIRCULAR ORBITS AND RADIATION REACTION

As discussed in the Introduction, the motion of the inspiraling body will be approximated in this analysis as a sequence of circular geodesic orbits. In this section, I briefly review first the characteristics of these orbits in the absence of radiation emission, and next the formalism by which the radiative corrections are computed. These results are the foundation for all of the analysis in this paper.

A. Geodesic orbits

Up to initial conditions, orbits of Kerr black holes are specified by choosing their energy E, axial angular momentum L_z, and Carter constant Q. Note that the values of these quantities used in this paper have been divided by the small body's mass μ (E and L_z) or μ^2 (Q) and are thus the specific energy, angular momentum and Carter constant. Having chosen these constants (and initial conditions), the orbit is then governed by geodesic equations for the small body's Boyer-Lindquist coordinates (t, r, θ, ϕ) as a function of proper time τ measured along the small body's worldline; see [43].

To describe circular orbits, it is useful to introduce the function $R \equiv \Sigma^2(dr/d\tau)^2$:

$$R = \left[E(r^2+a^2) - aL_z\right]^2 - \Delta\left[r^2 + (L_z - aE)^2 + Q\right] \ . \tag{2.1}$$

(The function $\Sigma = r^2 + a^2\cos^2\theta$, and $\Delta = r^2 - 2Mr + a^2$.) Circular orbits satisfy $R = 0$ and $R' = 0$; stable circular orbits satisfy in addition $R'' \leq 0$. Given the radius r and one of the three constants E, L_z, or Q, it is straightforward to solve the system $R = 0$, $R' = 0$ for the other two. When the hole is slowly rotating or the orbit is at large radius, it is generally most convenient to choose L_z and solve for E and Q:

$$E(r, L_z) = \frac{a^2L_z^2(r-M) + r\Delta^2}{aL_zM(r^2-a^2) \pm \Delta\sqrt{r^5(r-3M) + a^4r(r+M) + a^2r^2(L_z^2 - 2Mr + 2r^2)}} \ , \tag{2.2}$$

$$Q(r, L_z) = \frac{\left[(a^2+r^2)E(r,L_z) - aL_z\right]}{\Delta} - \left[r^2 + a^2E(r,L_z)^2 - 2aE(r,L_z)L_z + L_z^2\right] \ . \tag{2.3}$$

The sign choice in the denominator of Eq. (2.2) can cause problems when the spin is large and the orbit is at small radius. The positive sign is appropriate when $r > r_{\rm branch}(a)$, and the negative sign when $r < r_{\rm branch}(a)$, where $r_{\rm branch}(a)$ is the radius at which the argument of the square root is zero. For all values of a, $r_{\rm branch}(a) \sim 2M$. The difficulties associated with this sign choice can be avoided by choosing E and then solving for L_z and Q:

$$L_z(r,E) = \frac{EM(r^2-a^2) - \Delta\sqrt{r^2(E^2-1)+rM}}{a(r-M)} \ , \tag{2.4}$$

$$Q(r,E) = \frac{\left[(a^2+r^2)E - aL_z(r,E)\right]}{\Delta} - \left[r^2 + a^2E^2 - 2aEL_z(r,E) + L_z(r,E)^2\right] \ . \tag{2.5}$$

[Note that in Ref. [42], the a^2E^2 inside the second set of square brackets is incorrectly written a^2E.]

In practice, I have found it convenient to use Eqs. (2.4) and (2.5) to parameterize orbits that are located close to the set of marginally stable orbits (the orbits which satisfy $R=0$, $R'=0$, $R''=0$). When a small body spirals in, its orbit will become unstable when it crosses these orbits, rapidly plunging into the hole. The set of marginally stable orbits will be called the LSO (last stable orbits).

Orbits with $Q \neq 0$ are inclined with respect to the equatorial plane; a useful definition of the inclination angle ι is[3]

$$\cos\iota = \frac{L_z}{\sqrt{L_z^2+Q}} \ . \tag{2.6}$$

At a given radius r, two orbits bound the behavior of all stable circular orbits. The most-bound orbit is the prograde equatorial orbit ($\iota = 0$). Its constants are [44]

$$E^{\rm mb} = \frac{1-2v^2+qv^3}{\sqrt{1-3v^2+2qv^3}} \ , \tag{2.7}$$

$$L_z^{\rm mb} = rv\frac{1-2qv^3+q^2v^4}{\sqrt{1-3v^2+2qv^3}} \ , \tag{2.8}$$

$$Q^{\rm mb} = 0 \ , \tag{2.9}$$

where $v \equiv \sqrt{M/r}$ and $q \equiv a/M$. Prograde equatorial orbits exist at all radii outside $r_{\rm pro}$, where

$$r_{\rm pro}/M = 3 + Z_2 + \left[(3-Z_1)(3+Z_1+2Z_2)\right]^{1/2} \ , \tag{2.10}$$

$$Z_1 = 1 + \left[1-(a/M)^2\right]^{1/3}\left[(1+a/M)^{1/3} + (1-a/M)^{1/3}\right] \ , \tag{2.11}$$

$$Z_2 = \left[3(a/M)^2 + Z_1^2\right]^{1/2} \ . \tag{2.12}$$

This is also the radius of the LSO when $\iota = 0^\circ$ — no stable circular orbits exist inside $r_{\rm pro}$. If $r < r_{\rm ret}$, where

$$r_{\rm ret}/M = 3 + Z_2 + \left[(3-Z_1)(3+Z_1+2Z_2)\right]^{1/2} \ , \tag{2.13}$$

then the least-bound orbit is on the LSO, and the constants $(E^{\rm lb}, L_z^{\rm lb}, Q^{\rm lb})$ are found by numerically solving the system of equations $R=0$, $R'=0$, $R''=0$. If $r > r_{\rm ret}$, the least-bound orbit is the retrograde equatorial orbit ($\iota = 180^\circ$), and its constants are

$$E^{\rm lb} = \frac{1-2v^2-qv^3}{\sqrt{1-3v^2-2qv^3}} \ , \tag{2.14}$$

$$L_z^{\rm lb} = -rv\frac{1+2qv^3+q^2v^4}{\sqrt{1-3v^2-2qv^3}} \ , \tag{2.15}$$

$$Q^{\rm lb} = 0 \ . \tag{2.16}$$

Mapping out all stable circular orbits at some radius is thus fairly straightforward. First, calculate the constants that describe the most-bound orbit [Eqs. (2.7)–(2.9)]. Second, calculate the constants for the least-bound orbit [solving the system $R=0$, $R'=0$, $R''=0$ if $r < r_{\rm ret}$; using Eqs. (2.14)–(2.16) otherwise]. Finally, allow either E or L_z to vary between their most-bound and least-bound extremes. If varying L_z, use Eqs. (2.2) and (2.3) to get intermediate values; if varying E, use Eqs. (2.4) and (2.5).

---

[3]As discussed in Ref. [37], this angle does not necessarily accord with intuitive notions of inclination angle. For example, except when $a=0$, ι is *not* the angle at which most observers would see the small body cross the equatorial plane.

Circular orbits are periodic, with two (generally incommensurate) frequencies Ω_θ and Ω_ϕ, related to the small body's motion in the θ and ϕ coordinates. These two frequencies (and their harmonics) strongly stamp the gravitational waveform. A detailed derivation of these frequencies is given in Ref. [37]; the relevant results are as follows. First, define T_θ, the time it takes for the small body to execute its full range of θ motion as seen by infinitely distant observers. Its value is

$$T_\theta = \frac{4\gamma}{\sqrt{\beta z_+}} K\left(\sqrt{z_-/z_+}\right) + 4a^2 E\sqrt{\frac{z_+}{\beta}}\left[K\left(\sqrt{z_-/z_+}\right) - E\left(\sqrt{z_-/z_+}\right)\right] . \tag{2.17}$$

In this equation, $K(k)$ is the complete elliptic integral of the first kind, and $E(k)$ is the complete elliptic integral of the first kind. (Note that E with no argument is the orbit's energy.) The symbols γ and β are

$$\beta = a^2(1-E^2) , \tag{2.18}$$

$$\gamma = E\left[\frac{(r^2+a^2)^2}{\Delta} - a^2\right] + aL_z\left(1 - \frac{r^2+a^2}{\Delta}\right) ; \tag{2.19}$$

$z_\pm$ are defined by

$$\beta(z_+ - z)(z_- - z) = \beta z^2 - z\left[Q + L_z^2 + a^2(1-E^2)\right] + Q . \tag{2.20}$$

Next, define Φ as the azimuthal angle accumulated in one period T_θ. Its value is

$$\Phi = \frac{4}{\sqrt{\beta z_+}}\left[L_z \Pi\left(\pi/2, -z_-, \sqrt{z_-/z_+}\right) - \delta K\left(\sqrt{z_-/z_+}\right)\right] , \tag{2.21}$$

where $\Pi(\varphi, n, k)$ is the incomplete elliptical integral of the third kind (using the notation of [45]), and where

$$\delta = aE\left(\frac{r^2+a^2}{\Delta} - 1\right) - \frac{a^2 L_z}{\Delta} . \tag{2.22}$$

With these definitions, $\Omega_\theta = 2\pi/T_\theta$ and $\Omega_\phi = \Phi/T_\theta$.

B. Radiative corrections

The radiation reaction formalism used here is based on the Teukolsky equation [15], which governs the evolution of the complex Weyl curvature scalar related to radiative perturbations, ψ_4. This section briefly outlines how the radiative corrections are computed, particularly the quantities relevant to this analysis. Reference [37] discusses this material in greater detail.

The "master equation" for the evolution of ψ_4 is separated with the multipolar decomposition [15]

$$\psi_4 = \frac{1}{(r - ia\cos\theta)^4}\int_{-\infty}^{\infty} d\omega \sum_{lm} R_{lm\omega}(r)\, {}_{-2}S_{lm}^{a\omega}(\theta) e^{i(m\phi - \omega t)} . \tag{2.23}$$

The t and ϕ dependences are trivial (and follow from the fact that the background spacetime is stationary and axisymmetric). The function ${}_{-2}S_{lm}^{a\omega}(\theta)$ is a spin-weighted spheroidal harmonic. It is useful for describing the θ dependence of a radiation field with spin weight -2 in an oblate geometry. An effective algorithm for calculating this function is given in Appendix A of Ref. [37].

Computing the radial function $R_{lm\omega}$ takes some effort. This function obeys the Teukolsky equation:

$$\Delta^2 \frac{d}{dr}\left(\frac{1}{\Delta}\frac{dR_{lm\omega}}{dr}\right) - V(r) R_{lm\omega} = -\mathcal{T}_{lm\omega}(r) . \tag{2.24}$$

This equation is in self-adjoint form, and so can be solved with Green's functions [46]. The homogeneous Teukolsky equation has two independent solutions, $R^H_{lm\omega}(r)$ (which obeys the boundary condition that radiation must be purely ingoing at the event horizon) and $R^\infty_{lm\omega}(r)$ (which obeys the condition that radiation must be purely outgoing at infinity). From these solutions and from the source function $\mathcal{T}_{lm\omega}(r)$, one can write down the general solution $R_{lm\omega}(r)$:

$$R_{lm\omega}(r) = Z^H_{lm\omega} R^\infty_{lm\omega}(r) + Z^\infty_{lm\omega} R^H_{lm\omega}(r) \ . \tag{2.25}$$

A detailed description of how one computes $Z^H_{lm\omega}$, $Z^\infty_{lm\omega}$, $R^H_{lm\omega}$, and $R^\infty_{lm\omega}$ (and how they relate to the source function $\mathcal{T}_{lm\omega}$) is given in Ref. [37]. The most important details for this paper are as follows. First, for circular orbits, the source and all quantities derived from it are describable as harmonics of Ω_θ and Ω_ϕ. Defining

$$\omega_{mk} = m\Omega_\phi + k\Omega_\theta \ , \tag{2.26}$$

the functions $Z^H_{lm\omega}$ and $Z^\infty_{lm\omega}$ can be decomposed into harmonics:

$$\begin{aligned} Z^H_{lm\omega} &= \sum_k Z^H_{lmk} \delta(\omega - \omega_{mk}) \ , \\ Z^\infty_{lm\omega} &= \sum_k Z^\infty_{lmk} \delta(\omega - \omega_{mk}) \ . \end{aligned} \tag{2.27}$$

Second, as $r \to r_+ = M + \sqrt{M^2 - a^2}$ (the coordinate of the event horizon), $Z^H_{lm\omega} \to 0$ and $Z^\infty_{lm\omega} \to$ constant; as $r \to \infty$, $Z^\infty_{lm\omega} \to 0$ and $Z^H_{lm\omega} \to$ constant. It follows from this that the behavior at infinity of the radiation field and all related quantities depends only on Z^H_{lmk}:

$$h_+ - i h_\times = \sum_{lmk} \frac{Z^H_{lmk}}{\omega^2_{mk}} {}_{-2}S^{a\omega_{mk}}_{lm}(\theta) e^{i(m\phi - \omega_{mk} t)} \ ; \tag{2.28}$$

$$\begin{aligned} \left(\frac{dE}{dt}\right)^{\rm rad}_{r\to\infty} &= \sum_{lmk} \frac{|Z^H_{lmk}|^2}{4\pi\omega^2_{mk}} \ , \\ \left(\frac{dL_z}{dt}\right)^{\rm rad}_{r\to\infty} &= \sum_{lmk} \frac{m|Z^H_{lmk}|^2}{4\pi\omega^3_{mk}} \ . \end{aligned} \tag{2.29}$$

Likewise, the behavior at the horizon depends only on Z^∞_{lmk}:

$$\begin{aligned} \left(\frac{dE}{dt}\right)^{\rm rad}_{r\to r_+} &= \sum_{lmk} \alpha_{lmk} \frac{|Z^\infty_{lmk}|^2}{4\pi\omega^2_{mk}} \ , \\ \left(\frac{dL_z}{dt}\right)^{\rm rad}_{r\to r_+} &= \sum_{lmk} \alpha_{lmk} \frac{m|Z^\infty_{lmk}|^2}{4\pi\omega^3_{mk}} \ . \end{aligned} \tag{2.30}$$

(Note that, by assumption, the change in the orbital energy and angular momentum is opposite in sign to that radiated: $\dot{E}^{\rm orbit} = -\dot{E}^{\rm rad}$, $\dot{L}_z^{\rm orbit} = -\dot{L}_z^{\rm rad}$.) The factor α_{lmk} is a rather messy coefficient that follows from transforming the Kinnersley null tetrad (which is used to construct ψ_4 [47]) to the Hawking-Hartle null tetrad [48] (which is well behaved on the event horizon); see Ref. [37] for further details. As noted in [37], there is a symmetry relation between quantities at (l, m, k) and $(l, -m, -k)$:

$$Z^{H,\infty}_{l-m-k} = (-1)^{l+k} \bar{Z}^{H,\infty}_{lmk} \ . \tag{2.31}$$

This relationship can be used to reduce computation time — compute half the multipoles, use symmetry to get the other half. Alternatively, it can be used to improve computational accuracy — compute all the multipoles, use symmetry to reduce error:

$$Z^{H,\infty}_{lmk} = \frac{1}{2}\left[Z^{H,\infty}_{lmk;\,\rm comp} + (-1)^{l+k} \bar{Z}^{H,\infty}_{l-m-k;\,\rm comp}\right] \ . \tag{2.32}$$

This second approach was used in all computations here.

In computing $\dot{E}^{H,\infty}$ and $\dot{L}_z^{H,\infty}$, a large number of terms were included in the sums at all points. A detailed discussion of the truncation criterion used here is given in Sec. VA of Ref. [37]; in the language of that paper, the parameter $\epsilon_k = 10^{-4}$ and $\epsilon_l = 10^{-3}$. The truncation error in $\dot{E}^{H,\infty}$ and $\dot{L}_z^{H,\infty}$ is therefore roughly 10^{-3}. Obtaining this level of accuracy requiring summing to at least $l = 8$ (for innermost orbits of the $a = 0.998M$ black hole, the

sums were taken to $l = 19$); for each value of l, between 10 and 30 values of k were included. In all cases, the sum over m ranged from $-l$ to l.

As discussed in the Introduction, using the Teukolsky equation to compute $\dot{E}^{H,\infty}$ and $\dot{L}_z^{H,\infty}$ requires that the inspiral be adiabatic: over orbital timescales, the inspiral trajectory must be nearly geodesic. This requirement enters through the source term of the Teukolsky equation. This source term is built from the stress energy tensor of the small body in the Kerr spacetime, which is approximated as a delta function particle:

$$T_{\alpha\beta}(\mathbf{x}) = \mu \int d\tau \, u_\alpha u_\beta \, \delta^{(4)} \left[\mathbf{x} - \mathbf{z}(\tau)\right] \ . \tag{2.33}$$

Here, u_α is the orbiting body's 4-velocity, $\mathbf{x}$ is an arbitrary spacetime event, and $\mathbf{z}(\tau)$ is the body's worldline. This equation is the setup for a Catch-22: we need the worldline $\mathbf{z}(\tau)$ in order to compute the body's radiative corrections; however, the corrections determine that worldline! The solution is to approximate the worldline as geodesic for the purpose of computing the source term. We thus use the zeroth order (in μ/M) geodesic motion to compute the first order radiative corrections. This is a good approximation only when the radiative change in any orbital quantity χ over an orbit is much less than χ: $\dot{\chi} T_{\rm orb} \ll \chi$.

Very useful quantities to monitor are the orbital frequencies, Ω_ϕ and Ω_θ. Because $T_\theta = 2\pi/\Omega_\theta$, and defining $T_\phi = 2\pi/\Omega_\phi$, the adiabaticity condition for these quantities can be written

$$\mathcal{N}_\phi \equiv \frac{1}{2\pi} \frac{\Omega_\phi^2}{\dot{\Omega}_\phi} \gg 1 \ , \tag{2.34}$$

$$\mathcal{N}_\theta \equiv \frac{1}{2\pi} \frac{\Omega_\theta^2}{\dot{\Omega}_\theta} \gg 1 \ , \tag{2.35}$$

These parameters are closely related to the number of accumulated orbits in ϕ and θ:

$$\begin{aligned} N_{\phi,\theta} &= \frac{1}{2\pi} \int dt \, \Omega_{\phi,\theta} \\ &= \int d\ln \Omega_{\phi,\theta} \, \mathcal{N}_{\phi,\theta} \ . \end{aligned} \tag{2.36}$$

The adiabaticity condition $\mathcal{N}_{\phi,\theta} \gg 1$ tells us that the number of orbits accumulated by the inspiraling body as it passes through the orbital frequency band that is centered on $\Omega_{\phi,\theta}$ and of width $\delta\Omega_{\phi,\theta} = \Omega_{\phi,\theta}$ must be very large. More simply, adiabaticity requires that the body spend many orbits near any point in its orbital phase space.

One final point before moving on: the Teukolsky equation only tells us directly about the changes in E and L_z. It cannot be used directly to compute the change in Q. An additional constraint must be imposed in order to fully describe the small body's spiral in. Circularity provides this constraint. Adiabatic radiation reaction changes an orbit's radius and inclination angle, but it does not make the orbit eccentric [39–41] — circular orbits remain circular. Imposing the "circular goes to circular" rule leads to a relatively simple relationship between $(\dot{Q}, \dot{r})$ and $(\dot{E}, \dot{L}_z)$:

$$\begin{aligned} \dot{Q}^{H,\infty} &= m_{11} \dot{E}^{H,\infty} + m_{12} \dot{L}_z^{H,\infty} \ , \\ \dot{r}^{H,\infty} &= m_{21} \dot{E}^{H,\infty} + m_{22} \dot{L}_z^{H,\infty} \ . \end{aligned} \tag{2.37}$$

(Note that it is $\dot{E}^{\rm orbit}$ and $\dot{L}_z^{\rm orbit}$ that must be used on the right-hand side of this equation; the radiated changes have the wrong sign.) The (somewhat complicated) matrix elements m_{ij} are given in Eqs. (3.6a–e) of Ref. [37].

Letting χ stand for any of the quantities (E, L_z, Q, r), the total change in χ is found by summing the change due to radiation flux out to infinity and due to radiation flux down the event horizon:

$$\dot{\chi} = \dot{\chi}^\infty + \eta \dot{\chi}^H \ . \tag{2.38}$$

The parameter η (which clearly should equal 1) is introduced so that we can "turn off" the flux down the horizon. As we shall see later, setting $\eta = 0$ is a very interesting test of how strongly the black hole's event horizon influences inspiral. Note that from $\dot{Q}$ and $\dot{L}_z$ it is simple to compute the rate of change of the inclination angle ι (or rather $\cos\iota$):

$$\frac{d(\cos\iota)}{dt} = \frac{1}{\sqrt{L_z^2 + Q}} \left[\dot{L}_z - \frac{L_z}{2} \frac{2 L_z \dot{L}_z + \dot{Q}}{L_z^2 + Q} \right] \ . \tag{2.39}$$

The data $(\dot{r}, \dot{\iota})$ are the foundation of the inspiral trajectories discussed next.

III. COMPUTING INSPIRAL TRAJECTORIES AND WAVEFORMS

Using the techniques described in Sec. II, it is straightforward to compute the inspiral trajectory of a body orbiting a black hole and the gravitational waveforms generated in that inspiral. This is done in two steps. First, a "grid" of radiation reaction data is built in the phase space of allowed orbits in the black hole's strong field. The coordinates in this phase space are (r, ι). The radiation reaction data are the vectors along which gravitational-wave emission drives the orbital evolution, $(\dot{r}, \dot{\iota})$, plus the amplitude and frequency of the gravitational waveform, Z^H_{lmk} and ω_{mk}. I describe how this grid is built in Sec. III A. Next, the radiation reaction data are integrated to compute the inspiraling body's trajectory. The data are interpolated from discrete orbital coordinates on the grid to arbitrary points in the orbital phase space using a two dimensional cubic spline [45]. I briefly describe how this is done in Sec. III B.

A. Making a radiation reaction grid

Making a grid of radiation reaction data is for the most part straightforward. One discretizes the orbital phase space, choosing indices i and j such that radiation reaction data live at points (r_{ij}, ι_{ij}). Then, one uses the techniques summarized in Sec. II to compute the data. I describe here the algorithm used to discretize the orbital phase space, and also the actual form of the data (which are somewhat massaged so that they can be interpolated with as little error as possible).

After some experimentation, I have found it convenient to make the grid evenly spaced in radius, and evenly spaced *at each radius* in the orbital energy. The discretized radius is thus

$$r_{ij} \equiv r_j = r_{\rm min} + j\,\delta r\ . \tag{3.1}$$

The parameter $r_{\rm min}$ is chosen to be as close as is convenient to $r_{\rm pro}$ [cf. Eq. (2.10)]. In my calculations, I have set $r_{\rm min}$ to $r_{\rm pro}$, rounded up to the nearest $0.1M$. (This creates a small gap in data coverage near the LSO at small values of ι.) I have used $\delta r = 0.1M$ in all computations; as will be discussed shortly, more intelligent choices can be made. The index j can in principle be made arbitrarily large. For the results discussed in Secs. IV and V, I set $j_{\rm max} \sim 20 - 30$. For a $10^6\,M_\odot$ black hole and an inspiraling body with $\mu = 1\,M_\odot$, this leads to an inspiral lasting about 630 days — typical observation time for a LISA mission.

The discretized energy is

$$E_{ij} = E_{\rm mb} + (i-1)\delta E_j\ , \tag{3.2}$$

where $\delta E_j = \left[E_{\rm lb}(r_j) - E_{\rm mb}(r_j)\right]/(i_{\rm max} - 1)$. I have used $i_{\rm max} = 9$. The parameter space coordinates (r_j, E_{ij}) fully determine the orbit at grid point (i, j). Using the various relations given in Sec. II, we can remap this coordinate to any convenient parameterization. I will typically write the grid points as (r_j, ι_{ij}), with the understanding that this is a remapping from the grid coordinates (r_j, E_{ij}) that are directly generated.

A better choice for δr can be made by studying how Z^H_{lmk} is computed from solutions of the Teukolsky equation. From Eq. (4.8) of Ref. [37], we see that

$$Z^H_{lm\omega} \propto \int_{r_+}^{r} dr'\, R^H_{lm\omega}(r')\mathcal{T}_{lm\omega}(r')/\Delta(r')^2\ , \tag{3.3}$$

where r is the orbital radius, $R^H_{lm\omega}$ is the solution to the source-free Teukolsky equation that is purely ingoing at the event horizon, $\mathcal{T}_{lm\omega}(r)$ is the Teukolsky source term, and $\Delta(r) = r^2 - 2Mr + a^2$. The coefficient Z^H_{lmk} is then built from a harmonic decomposition of $Z^H_{lm\omega}$. The key point to note is that both $\mathcal{T}_{lm\omega}$ and Δ vary relatively slowly with respect to r. The function $R^H_{lm\omega}$, on the other hand, oscillates with a phase factor that is roughly e^{-ipr^*}, where

$$r^*(r) = r + \frac{2Mr_+}{r_+ - r_-}\ln\frac{r - r_+}{2M} - \frac{2Mr_-}{r_+ - r_-}\ln\frac{r - r_-}{2M}\ , \tag{3.4}$$

and where $p = \omega - m\Omega_H$, the mode frequency modified by the hole's spin frequency $\Omega_H = a/2Mr_+$ [cf. Eq. (4.4) of Ref. [37]]. The function $r^*(r)$ is the Kerr "tortoise coordinate", which often appears in studies of radiation propagation near black holes. Notice that dr^*/dr gets quite large near the black hole. Physically, this tells us that e^{-ipr^*} begins oscillating very rapidly as the horizon is approached. The phase of Z^H_{lmk} is likely to change by $\sim \pi$ radians over a lengthscale

$$\delta r^* \sim \frac{1}{p_{mk}} \,. \tag{3.5}$$

This suggests laying out the grid evenly spaced in r^*, or using a denser grid in r, which spacing

$$\delta r \simeq \left(\left| \frac{dr^*}{dr} \right| \right)^{-1} \frac{1}{|p_{LK}|} \,. \tag{3.6}$$

Here L is the maximum l index included in the calculation, and K is the maximum k index. This would create a grid that is far more densely sampled than that discussed here, especially for rapidly spinning holes. The rather crude choice $\delta r = 0.1M$ places strict limits on the accuracy of waveform generation in this analysis; as will be discussed in the Conclusion, this is an obvious starting point for improvements to this analysis.

Some care must be taken to put data on the grid that are useful for generating the inspiral trajectory. For the radiation reaction quantities, I have found it useful to store $d\cos\iota/dt$ and

$$[\cos\iota - \cos\iota_{\rm LSO}(r)]\,\dot{r} \equiv \dot{\rho} \,, \tag{3.7}$$

rather than $(\dot{r}, \dot{\iota})$. The quantity $d\cos\iota/dt$ is useful simply because it is more naturally related to the rates of change $\dot{L}_z$ and $\dot{Q}$. The quantity $\dot{\rho}$ on the other hand accounts for the fact that $\dot{r}$ diverges as the LSO is approached — the prefactor $\cos\iota - \cos\iota_{\rm LSO}(r)$ nicely clears out this divergence. This makes it possible for $\dot{r}$ to be very accurately interpolated from $\iota = 0°$ to $\iota_{\rm LSO}(r)$. For the gravitational waveform, the frequencies Ω_ϕ and Ω_θ are stored, as are the magnitude $\mathcal{A}_{lmk}$ and phase Φ_{lmk} of the complex amplitude,

$$Z^H_{lmk} = \mathcal{A}_{lmk} \exp(i\Phi_{lmk}) \,. \tag{3.8}$$

For equatorial orbits, $Z^H_{lmk} = 0$ when $k \neq 0$. The numerical code which computes Φ_{lmk} from Z^H_{lmk} erroneously assigns $\Phi_{lmk} = 0$ in this case. This is because the code cannot evaluate $\Phi_{lmk} = \arctan[{\rm Im}(Z^H_{lmk})/{\rm Re}(Z^H_{lmk})]$ in the limit $Z^H_{lmk} \to 0$. To get around this problem, $\Phi_{l,m,k\neq 0}$ is only stored for non-equatorial orbits. Near the equator, $\Phi_{l,m,k\neq 0}$ can then be computed quite well using extrapolation.

An example grid, for a hole with $a = 0.998M$, is shown in Fig. 1. The arrows in this plot represent the vector $(\dot{r}, \dot{\iota})$. Notice that the evolution gets more rapid as the LSO (represented by the dotted line) is approached — the arrows get longer, until finally the orbit becomes dynamically unstable and plunges into the hole. (The diverging vectors on the LSO have been suppressed in the figure, as they tend to overwhelm the rest of the data.) This grid prototypes all the radiation reaction data used in this paper — although differing in detail depending on the black hole spin, they have the general shape and layout shown in Fig. 1.

B. Integrating a trajectory across the grid

Radiation reaction data on the grid are used to build inspiral trajectories — the paths $[r(t), \iota(t)]$ that bodies follow as they spiral into the black hole. This is done with Euler's method: given a starting point $[r_0, \iota_0]$ and a time step δt, advance to $[r_0 + \dot{r}\,\delta t, \iota_0 + \dot{\iota}\,\delta t]$. It would be straightforward to use a more sophisticated stepping algorithm, such as a Runge-Kutta method, to improve the accuracy of the inspiral trajectory. For the purpose of a first exploration of extreme mass ratio inspiral properties, Euler's method is a good compromise between accuracy on the one hand, and code complexity and computational cost on the other. As the trajectory is built, other useful data are also calculated, particularly the accumulated number of orbits and the gravitational waveform.

The Euler method integration requires derivatives at arbitrary points in the orbital parameter space, which in turn requires smooth methods for interpolating off of the grid points. Linear interpolations turn out not to be adequate: discontinuities in the data's second derivative as grid boundaries are crossed noticeably affects the phasing of the computed gravitational waveform[4]. Two dimensional cubic spline interpolation [45] seems to produce an inspiral trajectory that is adequately smooth; it is used for all interpolations in this analysis.

The spline interpolation is done in the index coordinates, (i, j). Suppose we wish to interpolate data for some field χ onto (r, ι). First, we interpolate in j [which maps simply onto r; cf. Eq. (3.1)] for each value of i, yielding a one-index set of data at the radius r:

[4]The discontinuities are amazingly clear when one transforms a gravitational waveform so produced into audio data.

$$\text{Spline in } r: \qquad \chi_{ij} \mapsto \chi_i(r) \ . \tag{3.9}$$

Since all of the relevant data now live at a single radius, the index i maps onto $\cos\iota$. Interpolate in $\cos\iota$ to get the final data:

$$\text{Spline in } \cos\iota: \qquad \chi_i(r) \mapsto \chi(r,\iota) \ . \tag{3.10}$$

This procedure behaves very well with the radiation reaction data and waveform data discussed in Sec. III A.

The procedure for generating the inspiral trajectory and gravitational waveform now reduces to a simple recipe:

1. Pick a starting coordinate, $(r_0, \iota_0; t = 0)$.

2. Interpolate the data $d\cos\iota/dt$, $[\cos\iota - \cos\iota_{\rm LSO}]\,\dot{r} \equiv \dot{\rho}$, Ω_ϕ, Ω_θ, $\mathcal{A}_{lmk}$, and Φ_{lmk} onto this coordinate. Note that for the waveform amplitude and phase, this requires interpolations for every value of l, m, and k. This can become quite computationally intensive. As discussed in Sec. III A, Φ_{lmk} is not stored on the equator when $k \neq 0$. One gets data for $\Phi_{l,m,k\neq 0}$ between the equator and the next grid point by extrapolation. This works very well because, at constant radius, Φ_{lmk} is nearly flat as a function of $\cos\iota$.

3. Generate the gravitational waveform at that moment on the trajectory:

$$\begin{aligned}
&\omega_{mk} = m\Omega_\phi + k\Omega_\theta \ , \\
&h(t) \equiv h_+(t) - ih_\times(t) = \sum_{l=2}^{l_{\rm max}} \sum_{m=-l}^{l} \sum_{k=-k_{\rm max}}^{k=k_{\rm max}} \frac{\mathcal{A}_{lmk}}{\omega_{mk}^2} {}_{-2}S_{lm}^{a\omega_{mk}}(\vartheta) e^{i\Phi_{lmk}} e^{im\varphi} e^{-2\pi i(mN_\phi + kN_\theta)} \ .
\end{aligned} \tag{3.11}$$

   Formally, $l_{\rm max} = k_{\rm max} = \infty$. In practice, these numbers are truncated at something much smaller; I will show data for $l_{\rm max} = k_{\rm max} = 2$ and $l_{\rm max} = k_{\rm max} = 4$. The last term in $h(t)$ is a harmonic of the accumulated orbital phases; the factor in the exponential is equivalent to $-i\int dt(m\Omega_\phi + k\Omega_\theta)$. It would reduce to $-2\pi i(m\Omega_\phi + k\Omega_\theta)t$ if the orbital frequencies did not themselves evolve.

4. Compute the number of orbits accumulated so far:

$$\begin{aligned}
N_\phi(t+\delta t) &= N_\phi(t) + \Omega_\phi\,\delta t/2\pi \ , \\
N_\theta(t+\delta t) &= N_\theta(t) + \Omega_\theta\,\delta t/2\pi \ .
\end{aligned} \tag{3.12}$$

   Since the frequencies of ϕ and θ motion are generally incommensurate, these two numbers can be quite different.

5. Take an Euler step to a new coordinate:

$$\begin{aligned}
t_{\rm new} &= t_{\rm old} + \delta t \ , \\
r_{\rm new} &= r_{\rm old} + \frac{1}{\cos\iota - \cos\iota_{\rm LSO}} \dot{\rho}\,\delta t \ , \\
\cos\iota_{\rm new} &= \cos\iota_{\rm old} + \frac{d\cos\iota}{dt}\,\delta t \ .
\end{aligned} \tag{3.13}$$

6. Go to Step 2 and repeat. Continue until the inspiraling body crosses the LSO.

Results from applying this analysis to a large number of inspirals of black holes of various spins are discussed next.

IV. RESULTS: INSPIRAL TRAJECTORIES

Before generating inspiral trajectories and gravitational waveforms, we must choose a sample of black hole spins — the trajectories are unique for each spin choice of the massive black hole. (The effect of varying other parameters, particularly the mass and mass ratio, can be obtained by scaling.) The obvious goal here is to pick a range of a that allows us to see at least qualitatively the range of effects likely in astrophysical extreme mass ratio inspirals.

This analysis was done for four representative black hole spins: $a = 0.998M$, $a = 0.3594M$, $a = 0.8M$, and $a = 0.05M$. The first two spins were selected because they are rigorously calculable. The value $a = 0.998M$ is the "astrophysically maximal" value one finds when the black hole's mass and spin evolve due to thin disk accretion:

preferential capture of counter-rotating photons versus co-rotating photons buffers the spin at $0.998M$, preventing the hole from reaching the Kerr maximal value $a = M$ [49]. The second choice is the spin obtained by locking the rotation frequency of the horizon, $\Omega_H = a/2Mr_+$, to the orbital frequency of the innermost equatorial orbit at $r_{\rm pro}$, $\Omega = M/[r_{\rm pro}^{3/2} + aM^{1/2}]$. Equating these two frequencies and using Eq. (2.10) yields $a = 0.3594$. This spin might be obtained if at some point in the black hole's history strong magnetic fields threaded the event horizon and the inner edges of an accretion disk, torquing the hole such that its spin became locked to the disk's rotation [50]. The third choice, $a = 0.8M$, is primarily chosen because it breaks up the large gap between $0.998M$ and $0.3594M$. It is worth noting that this spin is in the range predicted by detailed models of black hole evolution in the presence of magnetohydrodynamic torque, such as are described in some models of quasar engines [51]. Finally, $a = 0.05$ is chosen to give an example of inspiral into a slowly spinning black hole. In all cases, the numbers presented are for a $\mu = 1\,M_\odot$ body spiraling into an $M = 10^6\,M_\odot$ black hole.

The results of this analysis are summarized in Figs. 2, 3, 6, 7, and 8. Before discussing the results for each of these cases, it is worthwhile to note some general trends in the data. The span of data in all cases has been chosen so that the total inspiral lasts about $630 - 650$ days for the shallowest inclination angles. Inspiral typically halts when the small body crosses the LSO; at the very shallowest inclination angles, it halts when the span of radiation reaction data ends (very close to the LSO).

The radius of the LSO as a function of inclination angle, $r_{\rm LSO}(\iota)$, depends quite strongly on the black hole spin — consider that for $a = 0$, $r_{\rm LSO}(\iota) = 6M$ independent of ι, whereas for $a = M$, $r_{\rm LSO}(0^\circ) = M$, $r_{\rm LSO}(180^\circ) = 9M$. Because of this, the starting radius of the inspiral is moved out to larger values as a is decreased. Also, the total number of starting inclination angles is less for large a: when a is close to M, trajectories that begin at high values of ι hit the LSO more quickly. Thus, in the data discussed below, inspiral into small a black holes occurs at larger coordinate radius than for large a, and more starting inclination angles are included in those data sets.

In all cases, I show the accumulated inspiral time, the number of orbits about the spin axis (N_ϕ) and the accumulated number of oscillations in θ (N_θ). As mentioned above, these numbers are easily scaled to different masses and mass ratios: the trajectory shapes are independent of the masses (provided the radial axis is r/M), and

$$T_{\rm inspiral} \propto \frac{M^2}{\mu}\,,$$
$$N_{\phi,\theta} \propto \frac{M}{\mu}\,. \tag{4.1}$$

The trajectories shown here thus apply for any black hole mass and any extreme mass ratio.

A. Trajectories for $a = 0.998M$

Trajectories for inspiral into a hole with spin $a = 0.998M$ are summarized in Fig. 2. This figure shows inspiral from $r = 4M$ into the LSO for several starting values of the inclination angle ι. The accumulated inspiral time, orbits about the spin axis, and number of oscillations in θ label each trajectory.

Notice that the trajectories are nearly flat — ι barely changes over the inspiral, decreasing somewhat as the small body passes through the very strong field. This decrease is contrary to weak-field expectations [37,39], and arises because the characteristics of Kerr geodesics become locked to the event horizon in the very strong field; see Ref. [42] for detailed discussion. The fact that the change in ι is so small is very interesting. The change turns out to be even smaller when a is not so large.

Figure 2 illustrates the true strong-field inspiral sequences predicted by general relativity, including the effect of radiation out to infinity and down the event horizon. An interesting experiment is to "turn off" the radiation down the horizon, setting the parameter η in Eq. (2.38) to 0. The inspiral trajectories found in this exercise are plotted in Fig. 3. Aside from turning off the horizon flux, these trajectories are computed with conditions identical to the trajectories plotted in Fig. 2. Notice that, particularly for shallow inclination angle ($\iota \lesssim 50^\circ$), the small body inspirals *more quickly* when the flux down the horizon is not included. The effect is quite significant: inspiral of the shallowest orbits is shortened by several weeks, orbiting $\sim 10^4$ fewer times when the horizon flux is ignored.

That the horizon flux tends to prolong the inspiral is, on first consideration, extremely surprising. Intuitively, one would guess that each flux would be an energy sink, so that each reduces the orbit's energy. Because of the hole's rapid rotation, this is not the case: the phenomenon of superradiance plays a major role. Superradiance is essentially a manifestation of the Penrose process — a radiation pulse incident on the black hole is backscattered with a gain in the pulse's energy [47]. The energy gain is at the expense of the hole's rotation — rotational kinetic energy is converted to radiative energy. Thus, when the hole spins rapidly enough, the horizon is a *source* of energy, not a sink.

A somewhat more physical picture of this phenomenon (which explains why the energy is transferred to the orbit, not simply radiated to infinity) can be put together based on work by James Hartle [52]. The portion of the Weyl tensor which describes "radiation down the event horizon" can be understood as the tidal field of the orbiting body acting on the black hole. This field distorts the horizon, raising a tidal bulge on the hole. The distortion can be quantified by computing the curvature of the horizon. Using formulas from Ref. [52], it is easy to show that the distortion is given by a sum over the coefficients Z^{∞}_{lmk} that in this analysis describe the radiation flux at the horizon.

The black hole's tidal bulge is equivalent to the bulge that the moon raises on the earth. When the rotation frequency of the hole is greater than the ϕ frequency, $\Omega_H > \Omega_\phi$, the hole's spin drags the bulge *ahead* of the orbiting body, in exactly the manner in which a tidal bulge on a viscous, fluid body is dragged by the body's rotation. (One can in fact interpret the horizon's behavior in terms of a viscous membrane [53].) In a reference frame that co-rotates with the small body's orbit, the bulge appears to lead the small body by some angle. This is illustrated in Fig. 4. Because the bulge leads the body, it exerts a torque that acts to increase the body's orbital velocity. The tidal bulge thus transfers the hole's rotational energy into the orbit, slowing the inspiral.

This picture predicts that the effect reverses if $\Omega_H < \Omega_\phi$. This in fact is exactly what we see.

As discussed in Sec. II B, it is important to monitor the adiabaticity parameters $\mathcal{N}_\phi$ and $\mathcal{N}_\theta$ during the inspiral. The values of $\mathcal{N}_\phi$ and $\mathcal{N}_\theta$ for the inspiral beginning at $\iota = 20^\circ$ are plotted in Fig. 5; $\mathcal{N}_\phi$ is plotted as the solid line, $\mathcal{N}_\theta$ is the dotted line. We see the adiabaticity condition $\mathcal{N}_{\phi,\theta} \gg 1$ is strongly satisfied everywhere except perhaps just before the end of inspiral. (This is because the inspiral rate sweeps up as inspiral proceeds, and can be regarded as a precursor to the final plunge.) The adiabaticity parameters scale with M/μ. This is a warning that the results of this code cannot be taken seriously if the mass ratio is not extreme enough: when $M/\mu \lesssim 1000$, the final stages of inspiral will not be adiabatic. An interesting feature in this plot is the divergence in $\mathcal{N}_\theta$ near $t = 470\,$days. This divergence occurs because $\dot{\Omega}_\theta$ switches sign there: the frequency stops increasing and begins decreasing. This will be discussed at greater length in Sec. V.

The adiabaticity parameters appear qualitatively as in Fig. 5 in all cases studied here (with the modification that the divergence in $\mathcal{N}_\theta$ only occurs for $a = 0.998M$). In the interest of brevity (and so as not to overwhelm the reader with data), no other sets of adiabaticity parameters will be shown.

B. Trajectories for $a = 0.3594M$

Trajectories for inspiral into a black hole with spin $a = 0.3594M$ are summarized in Fig. 6. These trajectories are set up in a similar manner as those for $a = 0.998M$; notable differences are that they begin at $r = 6.6M$, and more starting values of ι are included. The trajectories are even more flat in this case than they are when $a = 0.998M$. The inclination angle actually increases slightly in all cases (as weak-field analyses predict), but the amount of increase is too small to be noticeable on the figure.

Turning off the horizon flux does not have a very marked effect on inspiral for this spin, as can be seen by comparing the upper panel (horizon flux included) and lower panel (horizon flux ignored) of Fig. 6. This is essentially by construction: as described above, the spin $a = 0.3594$ is the value for which the horizon spin frequency matches the innermost orbital frequency. The lead angle between the tidal bulge and the orbiting body ranges from very small to nonexistent — as the body spirals through the innermost orbits, the bulge is nearly perfectly lined up with the body, exerting almost no torque on it. The small difference between the trajectories in the two panels is not surprising.

C. Trajectories for $a = 0.8M$

Inspiral trajectories for a black hole with $a = 0.8M$ are shown in Fig. 7. Not surprisingly, the properties of these trajectories are intermediate to those shown for the cases $a = 0.998M$ and $a = 0.3594M$. As in the case $a = 0.3594M$, the change in inclination angle is extremely small, increasing slightly.

This figure shows that inspiral is faster when the horizon flux is not included. This, again, is not a surprise: we expect that when $a = 0.8M$ the bulge raised on the event horizon leads the orbiting body, so that tidal coupling transfer energy from the hole's spin to the orbit. Although qualitatively the effect is the same as for the case $a = 0.998M$, quantitatively the effect is much smaller. The fractional change in the inspiral time is no more than about 1% when $a = 0.8M$, as opposed to 4.2% when $a = 0.998M$. Part of this is simply because the spin frequency of the hole is smaller when $a = 0.8M$ — the tidal bulge does not lead the orbiting body quite as much. Also, when $a = 0.8M$, the body's orbits never come as close to the event horizon as they do when $a = 0.998M$ — they reach the dynamical instability before they get so close. As a consequence, the tidal coupling is never as strong, and the integrated effect on the trajectory is relatively small.

D. Trajectories for $a = 0.05M$

Figure 8 shows trajectories for inspiral into a hole with $a = 0.05M$. The dependence of the inspiral properties on inclination angle is weak compared to the other cases examined, though definitely present. The change in the inclination angle is practically unnoticeable; the largest change (for inspiral near 90°) is $\delta\iota \simeq 0.007°$.

In this case, inspiral is quicker when the horizon flux is included. The horizon functions as a sink of energy, in accord with simple intuition: when the horizon flux is not included, the small body does not spiral in so quickly. Because the hole rotates so slowly, the tidal bulge raised on the horizon lags the orbiting body, and the torque that it exerts on the orbit tends to increase its inspiral rate. The magnitude of the effect is quite small (fractional change in inspiral time is about 0.1%).

V. RESULTS: GRAVITATIONAL WAVEFORMS

As the inspiral trajectory is generated, the gravitational waveform is constructed using Eq. (3.11). One example of such a waveform is shown in Fig. 9. This waveform is the + polarization generated during the inspiral beginning at $\iota = 40°$ into a hole with $a = 0.998M$; cf. Fig. 2. It is viewed in the hole's equatorial plane ($\theta = \pi/2$). The mass ratio used here is 10^{-4}; recall that 10^{-6} was used to make Fig. 2. The increase was to speed up the inspiral so that the amount of data generated in the wave was kept manageable. The waveform contains contributions from $l = 2, 3, 4$, and for $k = -4$ to 4.

Some of the interesting features of the waveform are apparent in Fig. 9. For example, the modulation of the "carrier" signal by the small body's motion in θ is quite apparent, as is the evolution of the signal frequencies. Some of these features are made even clearer by transforming the gravitational waveform into audio data and playing the gravitational-wave "sound". I have placed sounds corresponding to such gravitational-wave signals at the URL listed as Ref. [54]; the reader is invited to play these sounds and judge for themselves how clear are the various inspiral features. (In order for the sounds to lie within the frequency band to which human ears are sensitive — and also to keep the signal duration reasonable — the mass of the black hole is scaled down to $M \sim 100\,M_\odot$. Discussion of this and other technical points is given on the page listed in [54].)

The audio versions of the gravitational waveforms make it clear that, especially late in the inspiral, the gravitational waveforms take the form of *multi-voice chirps*. Strong radiation is emitted at multiple harmonics of the inspiral frequencies; each harmonic plays the role of a separate "voice" in the "chorus" that constitutes the overall waveform. This multi-voice structure is in fact apparent in the form of the gravitational wave, Eq. (2.28), and can be made clearer by writing the waveform as follows:

$$\begin{aligned} h(t;\vartheta,\varphi) &\equiv h_+(t;\vartheta,\varphi) - i h_\times(t;\vartheta,\varphi) \\ &= \sum_{l=2}^{l_{\max}} \sum_{m=-l}^{l} \sum_{k=-k_{\max}}^{k_{\max}} \mathcal{H}_{lmk}(t;\vartheta) \exp\left[i\Psi_{lmk}(t;\varphi)\right] \ . \end{aligned} \tag{5.1}$$

Here, ϑ is the angle between the observer's line of sight and the black hole's spin axis; φ is the value of the inspiraling body's ϕ coordinate when $t = 0$ (assuming the coordinate system is defined such that the observer is at $\phi = 0$). Comparing with Eq. (3.11), we read off the values of the wave amplitude $\mathcal{H}_{lmk}$ and phase Ψ_{lmk} in terms of quantities directly computable from the Teukolsky equation:

$$\mathcal{H}_{lmk}(t;\vartheta) = \mathcal{A}_{lmk-2} S_{lm}^{a\omega_{mk}}(\vartheta)/\omega_{mk}^2 \ . \tag{5.2}$$

$$\begin{aligned} \Psi_{lmk}(t;\varphi) &= \Phi_{lmk} + m\varphi - 2\pi(mN_\phi + kN_\theta) \ , \\ &= \Phi_{lmk} + m\varphi - \int_0^t dt' \left(m\Omega_\phi + k\Omega_\theta\right) \ . \end{aligned} \tag{5.3}$$

[Recall Eq. (3.8), defining $\mathcal{A}_{lmk}$ and Φ_{lmk}.] The last line emphasizes that a big portion of the phase accumulated is nothing more than the integrated orbital phases.

Presenting the waveform in this way gives a very good sense of which harmonics are likely to contribute strongly to a gravitational-wave measurement. As will be shown in Secs. V A and V B, the phase evolution for each voice is very simple, though their summed effect is typically rather complicated (cf. the summed waveform shown in Fig. 9). This suggests that searching for each individual voice may be more effective than searching for the entire waveform. An effective way of implementing such a search might be developed using the "Fast Chirp Transform" (FCT) of Jenet and Prince [55]. The FCT is a generalization of the Fast Fourier Transform (FFT; see, e.g., Ref. [45] and references

therein). The FFT provides an efficient computational implementation of a Fourier transform — a decomposition of data onto basis functions $e^{2\pi i f t}$. These basis functions have phases that grow linearly with time. The FCT generalizes this to decompose data onto functions whose phases do not vary linearly with respect to time. The phase behavior of the basis functions $e^{i\Phi_{\rm FCT}(t)}$ must be specified by some model; indications are that it works well for a wide-variety of smoothly varying phase behaviors. Although further investigation is needed to test this idea, the voices of extreme mass ratio inspiral are good candidates for detection with the FCT.

The waveform results I presented here are restricted to the cases $a = 0.998M$ and $a = 0.3594M$. The results for these spin values contain enough interesting structure to draw some useful conclusions about extreme mass ratio gravitational waves.

A. Waveforms for $a = 0.998M$

Discussion in this section will focus on waves generated during an inspiral that starts at $\iota = 20°$ (cf. Fig. 2). All waveform data shown corresponds to waves measured in the hole's equatorial plane.

Figure 10 shows the wave amplitudes $\mathcal{H}_{lmk}$ and phases Ψ_{lmk} for $l = 2$, $m = 2$, and $k \in [0, 1, 2, 3, 4]$. Several features are worth noting in this plot. First of all, notice that the accumulated phase Ψ_{22k} for all values of k is quite large — the number of accumulated radians ranges from about 8×10^4 to 1.1×10^5. The accumulated phase scales inversely with the mass ratio, so the accumulated phase in these harmonics would be $\sim 10^7$ radians for a mass ratio of 10^{-6} (as was used in Figs. 2, 6, 7, 8). It is by tracking the phase over this large number of radians that it will be possible to determine the characteristics of the black hole spacetime with very high accuracy.

Second, notice that the strongest waves are emitted in the $k = 0$ harmonic. Indeed, the $l = 2$, $m = 2$, $k = 0$ voice turns out to be the strongest one present among the various harmonics that contribute to the gravitational waveform. This is the result one would have expected from the fact that the dominant contribution to the emitted gravitational waves is quadrupolar. Note, though, that the $k = 1$ harmonic becomes almost as strong as the $k = 0$ voice late in the inspiral. This is another generic feature of the multi-voice chirps: late in the inspiral, when waves are emitted from very deep in the black hole's strong field, harmonics which were not initially very important can contribute strongly to the gravitational waveform.

Finally, notice that the lines corresponding to $k = 2$, $k = 3$ and $k = 4$ "crash" and behave rather oddly late in the inspiral. This is a resolution problem caused by the crude manner with which I have discretized the orbital parameter space — constant Boyer-Lindquist radial steps with $\delta r = 0.1M$. In this region $p_{mk} \sim (0.2 - 0.5)/M$, and $|dr^*/dr| \sim 30 - 40$. Following the discussion near Eq. (3.6) above, the choice $\delta r = 0.1M$ is not really sufficient to follow the phase variation of Z^H_{lmk}; decreasing the step by a factor of 2 to 5 would vastly improve this analysis.

The behavior of the radiating harmonics for $l = 2$, $m = 0$ is plotted in Fig. 11. Notice that the phase actually *decreases* at late times. This is because the strongest contributor to the phase evolution of these waves is the frequency Ω_θ, which begins decreasing at late stages of the inspiral. We have already seen this behavior — recall that the adiabaticity parameter $\mathcal{N}_\theta$ diverges at the moment that $\dot{\Omega}_\theta = 0$ (cf. Fig. 5). The evolution of both Ω_θ and Ω_ϕ are shown in the upper panel of Fig. 12. The decrease in Ω_θ occurs because, when $a = 0.998M$, the small body orbits very close to the event horizon towards the end of inspiral. As a consequence, its θ motion is highly redshifted as seen by distant observers. (The ϕ frequency, by contrast, is not so redshifted; instead, it tends to the hole's spin frequency as the orbit becomes locked to the dragging of inertial frames.) The frequencies for inspiral into a hole with $a = 0.3594M$ exhibit no such unusual behavior; at all times, the inspiraling body is so far from the horizon that there is no significant redshift effect.

Observation of this decreasing frequency would be a wonderful probe of the black hole's strong field properties: a "reverse chirp" can only occur for orbits that get very close to the event horizon, and so would be a strong signature of the horizon. Unfortunately, the reversal in the phase evolution coincides with a rather rapid decrease in amplitude for these voices, as can be seen by comparing the upper and lower panels of Fig. 11. As the frequency gets smaller, the rate of change of source multipole moments associated with that frequency decreases. Since the variation in these multipoles directly determines the wave amplitude, it is guaranteed that any voice with a decreasing frequency will likewise have a decreasing amplitude [56].

Although the waveform's strongest radiation is emitted in voices corresponding to $l = 2$, $m = 2$, the voices corresponding to $l = m$, $m \neq 2$ are also quite strong, particularly at late times. The example $l = 4$ is plotted in Fig. 13. At the end of inspiral, $l = 4$, $m = 4$, $k = 0$ voice is about one fifth as strong as the $l = 2$, $m = 2$, $k = 0$ voice.

B. Waveforms for $a = 0.3594M$

I again focus on waves generated during inspiral beginning at $\iota = 20°$ (cf. Fig. 6). Discussion here will be for one set of voices only, $l = 2$, $m = 2$, and $k \in [0, 1, 2, 3, 4]$; only data in the hole's equatorial plane is used.

The phases and amplitudes of these voices are plotted in Fig. 14. For the most part, their behavior is similar to those for the waveform voices when $a = 0.998M$. For example, the voice corresponding to $k = 0$ is the strongest here, just as when $a = 0.998M$. One notable difference in this case is that no other voices become very strong towards the end of inspiral — when the inspiral ends, the $k = 1$ voice is about a factor of 10 weaker than the $k = 0$ voice. Also, we see that the code was able to reliably compute all voices except the one corresponding to $k = 4$. This is because the frequencies are quite a bit lower in this case, and also $|dr^*/dr| \lesssim 1.7$ over the inspiral domain. The grid spacing $\delta r = 0.1M$ work well, except for large harmonic indices.

In order to keep the number of figures in this paper from swelling any further, I will not present any other waveform data for $a = 0.3594M$. Two important points that could be seen in those data are as follows: first, because Ω_θ grows monotonically, no voices fade away, in contrast to the $l = 2$, $m = 0$ voices for $a = 0.998M$. Second, other values of l become stronger late in the inspiral, though not as interestingly as when $a = 0.998M$. At the end of inspiral the $l = 4$, $m = 4$, $k = 0$ voice is about one twentieth the strength of the $l = 2$, $m = 2$, $k = 0$ voice.

VI. CONCLUSION: IMPLICATIONS FOR LISA SOURCES

The results presented here give the first strong-field gravitational waveforms for rigorously computed extreme mass ratio inspiral trajectories. Because these trajectories are restricted to zero eccentricity, they do not correspond to inspirals that LISA is likely to observe. Nonetheless, they contain interesting features that are very likely to be present in the general case, and are certainly worthy of further study.

One of the most interesting features of these extreme mass ratio inspiral waves is their "multi-voice" structure: each (l, m, k) harmonic follows its own phase and amplitude evolution. The total waveform is given by the sum of the various voices as the inspiral progresses. Provided inspiral is adiabatic, this multi-voice structure should describe generic inspiral waves as well (albeit with a third index describing harmonics of the radial frequency Ω_r).

It should be possible to take advantage of the multi-voice structure of extreme mass ratio inspirals when developing strategies for analyzing the LISA datastream. Searches of the datastream for ground-based gravitational-wave detectors such as LIGO will rely in many cases on matched filtering, a technique that cross-correlates the instrumental data with templates of a source's full gravitational waveform, $h(t)$. Matched filtering functions particularly well when the template accurately models the source's phase evolution; accurate models for the amplitude are far less important. When searching for extreme mass ratio signals, then, it may be easier to search for each voice with its rather simple phase evolution, $h_{lmk}(t) = \mathcal{H}_{lmk}(t)e^{i\Psi_{lmk}(t)}$, than to search for the entire "chorus", $h(t) = \sum h_{lmk}(t)$, with its comparatively complicated phase evolution. Indeed, some signals might only be detectable in their higher harmonics — one can imagine using the $m = 4$ voices to find inspiral into holes so massive that the $m = 2$ harmonics are at frequencies too low to be seen. Techniques that look for extreme mass ratio inspirals on a voice-by-voice basis should have no problem finding those inspirals, provided these high-harmonic voices are not too weak. The Fast Chirp Transform developed by Jenet and Prince [55] may be a computationally effective means of implementing such a voice-by-voice search.

In this vein, it is interesting to note that the phase evolution of each voice is dominated by that voice's integrated frequency. Recall, from Eqs. (2.28), (5.1), (5.2) and (5.3) that the evolving phase consists of two pieces. One piece amounts to an integral of that voice's frequency, ω_{mk}; the other corresponds to the phase of the complex amplitude Z^H_{lmk} at a given moment during the inspiral:

$$\Psi_{lmk}(t) = \int_0^t dt'\, \omega_{mk}[r(t'), \iota(t')] + \Phi_{lmk}[r(t), \iota(t)] \,. \tag{6.1}$$

(I'm ignoring here the constant $m\varphi$ contribution to each voice, which essentially describes initial conditions at the moment measurement begins.) As the body inspirals, the contribution from the integrated frequency contributes $\sim 10^5 - 10^7$ radians to the phase evolution. By contrast, the phase Φ_{lmk} does not accumulate nearly as many radians, as shown in Fig. 15 — the change in Φ_{lmk} is generally less than a few tens of radians. This suggests that accurately calculating the inspiral trajectory, and hence having good information about the evolution of the orbital frequencies, is likely to be more important than knowing Φ_{lmk}.

The influence of tidal coupling between the inspiraling body and the black hole is very robust and interesting — such coupling will strongly influence the rate of inspiral regardless of the orbital parameters. If nature provides black holes

that rotate sufficiently fast, the prolonging of inspiral due to this coupling will easily be seen in the gravitational-wave data. This is a clean, beautiful probe of the strong-field black hole spacetime.

The analysis presented here suggests several possible directions for future work:

- Equatorial orbits. Glampedakis and Kennefick [38] are currently finishing an analysis of radiation reaction on eccentric, equatorial orbits of Kerr black holes; it is an analysis equivalent to that done in Ref. [37]. The radiation reaction data they develop could be used to duplicate this analysis but to find inspiral sequences for eccentric, equatorial orbits and to develop the associated inspiral waveforms. It would be quite valuable to have results that include the effect of eccentricity and modulations induced by the radial frequency Ω_r.

- Generic orbits. We can in principle calculate gravitational waves from generic orbits of Kerr black holes — all we need to do is specify the source term for a particular orbit in the Teukolsky equation (2.24) and solve. However, we are hampered by our inability to compute the backreaction on such orbits. Nonetheless, we may get valuable insight by imposing physically motivated constraints in order to generate an approximate inspiral trajectory. The trajectories presented here indicate that the change in inclination angle is very small (particularly when $a < 0.998M$). Using the Teukolsky equation to compute $\dot{E}$ and $\dot{L}_z$ from the gravitational-wave flux and imposing $\dot{\iota} = 0$ is sufficient to fully compute the inspiral trajectory through the generic orbit parameter space (r, e, ι). The gravitational waves developed in such a study would be valuable tools for exploring the influence of all three orbital frequencies $(\Omega_\phi, \Omega_\theta, \Omega_r)$ on the gravitational waveform.

- Improved waveforms. As discussed in Sec. III A, the parameter space discretization was used here was rather crude. It was in fact insufficient to accurately compute the amplitudes and phases of high frequency contributions to the waveforms shown here. As work begins to develop data analysis tools for LISA, this analysis should be refined so that simple limitations such as this discretization are unimportant. Also, the parameter space covered in this analysis is rather inadequate for studying LISA measurements. The range covered here was selected simply for computational convenience. A better analysis would chose the parameter space covering to span a range of inspirals corresponding to the masses and observation times that LISA is likely to measure.

Implementing the above items will put on us well on the way to understanding the data analysis problem with LISA. Having a broader set of accurate waveforms will serve as a very useful testbed for developing analysis tools and for getting a better understanding of how measureable extreme mass ratio signals are likely to be.

ACKNOWLEDGMENTS

I am indebted to Daniel Kennefick for many useful conversations and advice, particularly during the writing of the numerical code used in this analysis. I also thank Lee Lindblom for asking a question which led me to begin investigating the inspiral trajectories, Sam Finn for suggesting that the multi-voice decomposition shown in Eq. (5.1) should be analyzed, and Amy Hughes for helping develop some of the software used to process the numerical data shown here. I also thank Lior Burko, Curt Cutler, Yuri Levin, Sterl Phinney, and Kip Thorne for many useful discussions. All of the numerical code used in this analysis was developed with tools from the Free Software Foundation; all plots were generated with the package SM. This research was supported at the ITP by NSF Grant PHY-9907949 and at Caltech by NSF Grants AST-9731698 and AST-9618537, and NASA Grants NAG5-6840 and NAG5-7034.

---

[1] K. Danzmann *et al.*, *LISA — Laser Interferometer Space Antenna, Pre-Phase A Report*, Max-Planck-Institut für Quantenoptik, Report MPQ 233 (1998).
[2] E. E. Flanagan and S. A. Hughes, Phys. Rev. D **57**, 4525 (1998).
[3] S. Sigurdsson and M. J. Rees, Mon. Not. R. Astron. Soc. **284**, 318 (1997).
[4] S. Sigurdsson, Class. Quantum Grav. **14**, 1425 (1997).
[5] M. Freitag, unpublished Ph. D. thesis, Université de Genève, 2000, Chap. 4.
[6] One way to estimate the eccentricity when the system enters the LISA band is to use Newtonian orbital dynamics and quadrupole order gravitational radiation reaction. First take "initial" orbital parameters as described in Ref. [5] (cf. that reference's Fig. 4.52). Then, find the "final" orbital semi-major axis by requiring the system to enter LISA's frequency band. Formulas given in Ref. [7] then provide the eccentricity when the system becomes visible to LISA. The range quoted

in the text was obtained by looking at initial orbital parameters in the range given by Freitag, and for black hole masses in the range $10^5 - 10^7\,M_\odot$. (This mass variation is a somewhat strong abuse of Freitag's results, since he allows his black hole to grow substantially during a computation. However, the lesson that eccentricity is rapidly shrunk until it is in the ballpark of 0.5 seems universal.)
[7] P. C. Peters, Phys. Rev. **136**, B1224 (1964).
[8] F. D. Ryan, Phys. Rev. D **56**, 1845 (1997).
[9] R. Narayan, Astrophys. J. **536**, 663 (2000).
[10] E. Quataert and A. Gruzinov, Astrophys. J. **549**, 809 (2000).
[11] G. H. Ball, R. Narayan, and E. Quataert, to appear in Astrophys. J.; also astro-ph/0007037.
[12] G. Fodor, C. Hoenselaers, and Z. Perjés, J. Math. Phys. **30**, 2252 (1989).
[13] F. J. Ernst, Phys. Rev. **167**, 1175 (1968).
[14] F. D. Ryan, Phys. Rev. D **52**, 5707 (1995).
[15] S. A. Teukolsky, Ap. J. **185**, 635 (1973).
[16] S. A. Hughes, Phys. Rev. D **62**, 044029 (2000).
[17] W. G. Dixon, in *Isolated Gravitating Systems in General Relativity*, edited by J. Ehlers (Amsterdam, North Holland, 1978).
[18] J. Levin, Phys. Rev. Lett. **84**, 3515 (2000).
[19] J. Levin, Phys. Rev. D, submitted; also gr-qc/0010100
[20] M. Hartl and E. S. Phinney, in preparation.
[21] Lior Burko has emphasized (L. M. Burko, private communication) that this force also includes a non-dissipative component that can change the properties of the orbit itself. This component of the force arises physically from the self-interaction of the body with its gravitational field, and should induce effects that scale with the small body's mass squared.
[22] Y. Mino, M. Sasaki, and T. Tanaka, Phys. Rev. D **55**, 3457 (1997).
[23] T. C. Quinn and R. M. Wald, Phys. Rev. D **56**, 3381 (1997).
[24] Y. Mino, in preparation. See also talk presented at the 3rd Capra Ranch Meeting, Caltech, June 2000 (online proceedings available at `www.tapir.caltech.edu/~capra3`).
[25] A. G. Wiseman, Phys. Rev. D **61**, 084014 (2000).
[26] A. Ori, Phys. Rev. D **55**, 3444 (1997).
[27] L. Barack and A. Ori, Phys. Rev. D **61**, 061502 (2000).
[28] L. M. Burko, Phys. Rev. Lett. **84**, 4529 (2000).
[29] C. Lousto, Phys. Rev. Lett. **84**, 5251 (2000).
[30] W. G. Anderson, E. E. Flanagan, and A. C. Ottewill, in preparation.
[31] S. Detweiler, Phys. Rev. Lett. **86**, 1931 (2001).
[32] H. Nakano, Y. Mino, and M. Sasaki, Phys. Rev. D, submitted; also gr-qc/0104012.
[33] E. Poisson, Phys. Rev. D **47**, 1497 (1993).
[34] C. Cutler, L. S. Finn, E. Poisson, and G. J. Sussman, Phys. Rev. D **47**, 1511 (1993).
[35] T. A. Apostolatos, D. Kennefick, A. Ori, and E. Poisson, Phys. Rev. D **47**, 5376 (1993).
[36] Y. Mino, M. Sasaki, M. Shibata, H. Tagoshi, and T. Tanaka, Prog. Theor. Phys. Suppl. **128** (1997), Chap. 1.
[37] S. A. Hughes, Phys. Rev. D **61**, 084004 (2000); **63**, 049902(E) (2001).
[38] K. Glampedakis and D. Kennefick, in preparation.
[39] F. D. Ryan, Phys. Rev. D **53**, 3064 (1996).
[40] D. Kennefick and A. Ori, Phys. Rev. D **53**, 4319 (1996).
[41] Y. Mino, unpublished Ph. D. thesis, Kyoto University, 1996.
[42] S. A. Hughes, Phys. Rev. D **63**, 064016 (2001).
[43] C. W. Misner, K. S. Thorne, J. A. Wheeler, *Gravitation* (Freeman, San Francisco, 1973), Chap. 33.
[44] J. M. Bardeen, W. H. Press, and S. A. Teukolsky, Astrophys. J. **178**, 347 (1972).
[45] W. H. Press, S. A. Teukolsky, W. T. Vetterling, and B. P. Flannery, *Numerical Recipes* (Cambridge University Press, Cambridge, 1992).
[46] G. Arfken, *Mathematical Methods for Physicists* (Academic Press, Orlando, 1985), Chap. 16.
[47] W. H. Press and S. A. Teukolsky, Astrophys. J. **193**, 443 (1974).
[48] S. W. Hawking and J. B. Hartle, Commun. Math. Phys. **25**, 283 (1972).
[49] K. S. Thorne, Astrophys. J. **191**, 507 (1974).
[50] R. D. Blandford, private communication.
[51] R. Moderski, M. Sikora, and J.-P. Lasota, Mon. Not. R. Astron. Soc. **301**, 142 (1998).
[52] J. B. Hartle, Phys. Rev. D **9**, 2749 (1974).
[53] K. S. Thorne, R. H. Price, and D. H. MacDonald, *Black Holes: The Membrane Paradigm* (Yale University Press, New Haven, CT, 1986).
[54] Audio representations of these and other gravitational waveforms, in Sun `.au` format, can be obtained from the URL `http://www.tapir.caltech.edu/~hughes/Research/RRKerr/wave_spec.html`. Instructions for playing these sounds are given at that URL; please contact the author if you have any technical difficulties.
[55] F. A. Jenet and T. A. Prince, Phys. Rev. D **62**, 122001 (2000).

[56] In several talks, I have claimed that the amplitude associated with the decreasing frequency will actually be rather large. This was entirely *wrong*. My statement was based on an earlier stage of this analysis; at the time, the code which interpolates from the parameter space grid to arbitrary parameter space coordinates had a significant bug, which introduced a strong, backward chirping component into the waveform.

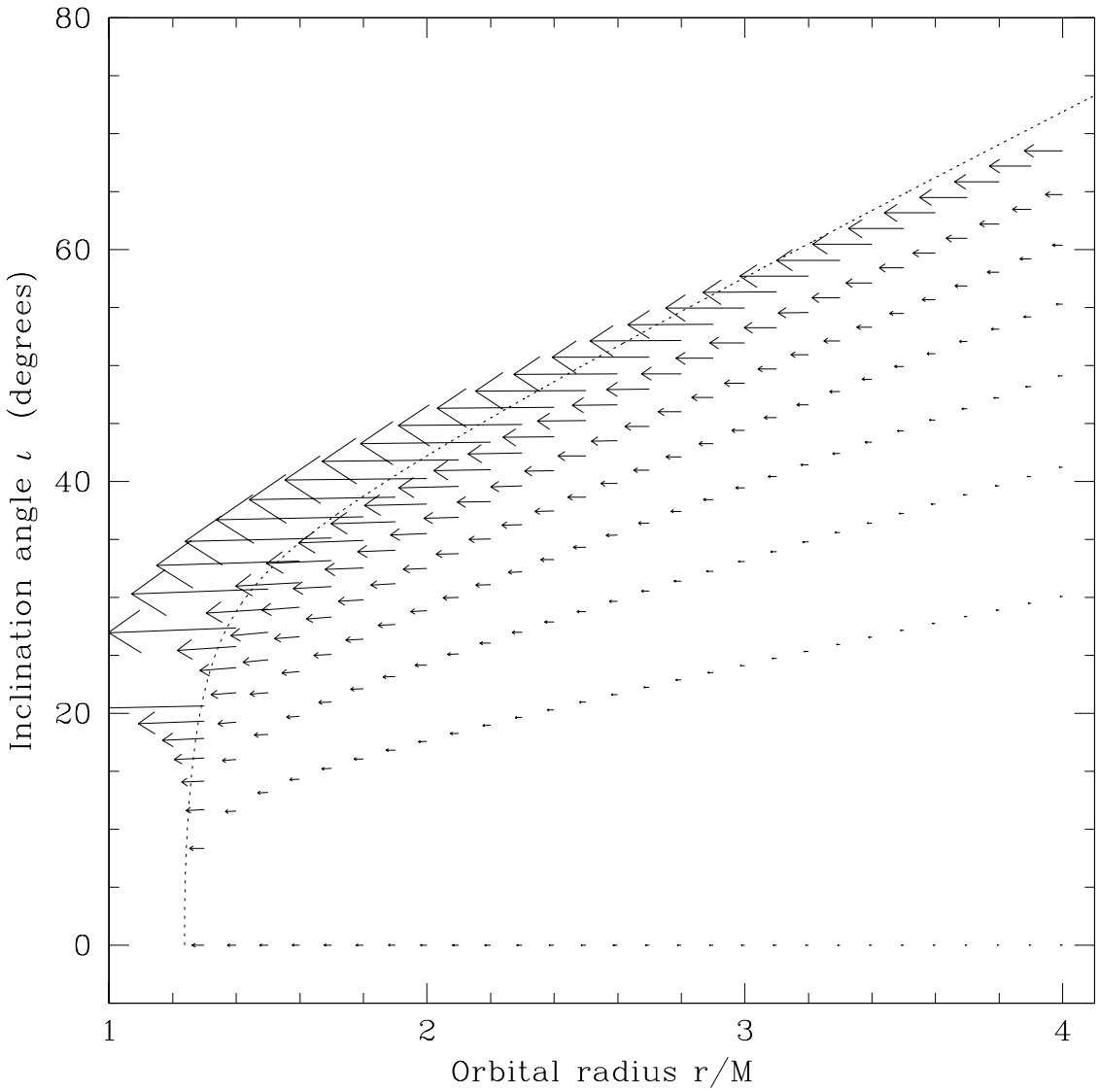

FIG. 1. A grid of circular orbit radiation reaction data near the last stable orbits (LSO) of a Kerr black hole with $a = 0.998M$. Any point (r, ι) in this plot is a circular geodesic orbit. The arrows are proportional to the vector $[(M/\mu)\dot{r}, (M^2/\mu)\dot{\iota}]$: the orientation gives the direction in which gravitational-wave emission drives the orbit, and the magnitude is proportional to the rate at which it is so driven. The dotted line represents the LSO — orbits above and to the left of this line are unstable to small perturbations and rapidly plunge into the black hole. The arrows get longer as this line is approached and their dynamical stability decreases. (Additional data were produced representing radiation reaction for orbits on the LSO; these orbits are so unstable that their radiation reaction vectors do not fit on this plot. These data are used in all computations, however.)

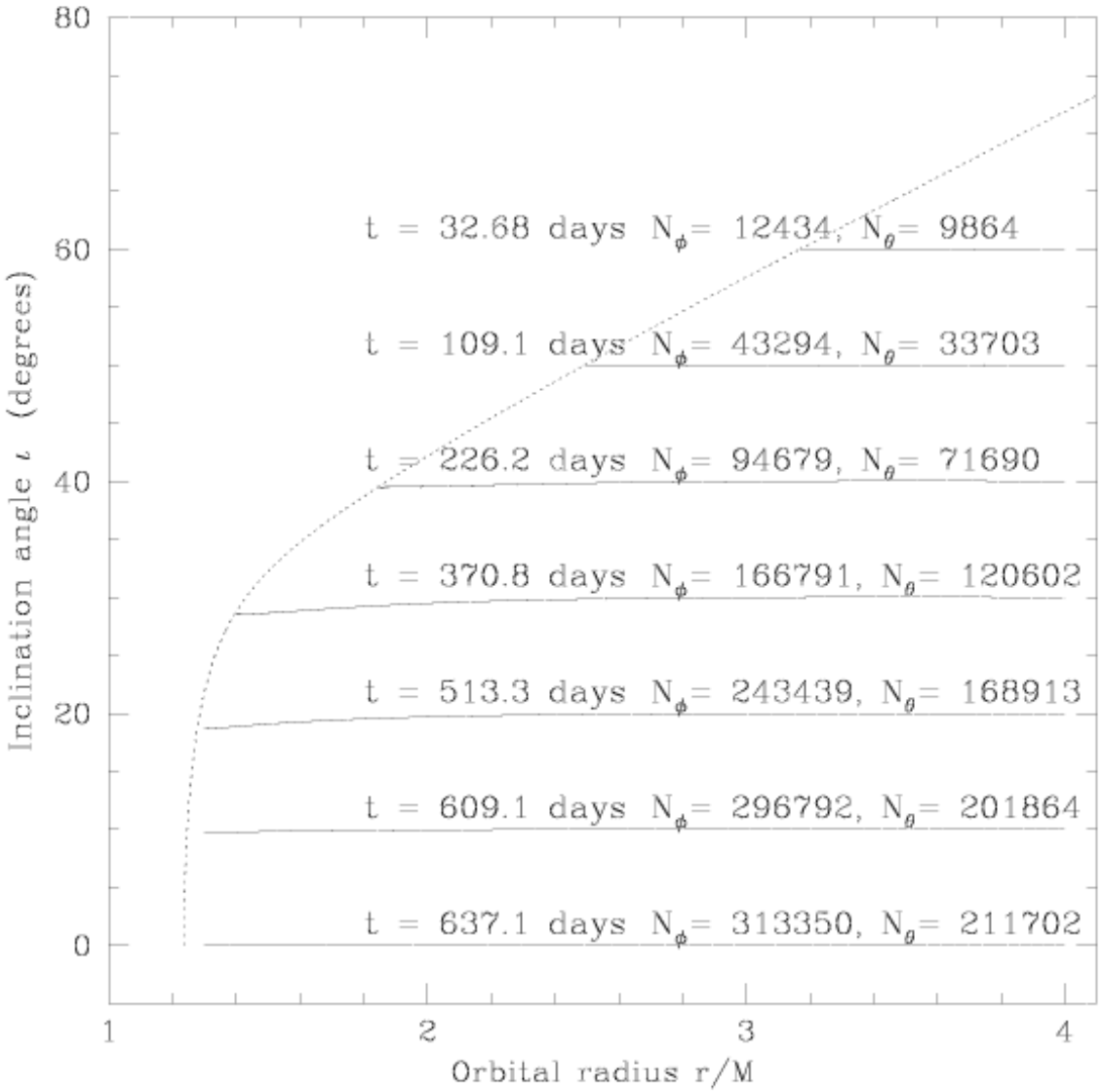

FIG. 2. Inspiral trajectories in the strong field of a Kerr black hole with $a = 0.998M$. To make this plot, the data shown in Fig. 1 were integrated using the procedures discussed in Sec. III B, assuming that the black hole has mass $M = 10^6\,M_\odot$ and that the inspiraling body has mass $\mu = 1\,M_\odot$. The trajectory shapes are independent of the two masses, so the inspiral times and accumulated number of cycles $N_{\phi,\theta}$ can be rescaled to other masses quite easily: $T_{\rm inspiral} \propto M^2/\mu$, $N_{\phi,\theta} \propto M/\mu$. Notice that the trajectories are nearly flat — ι decreases, but not very much, over these inspirals.

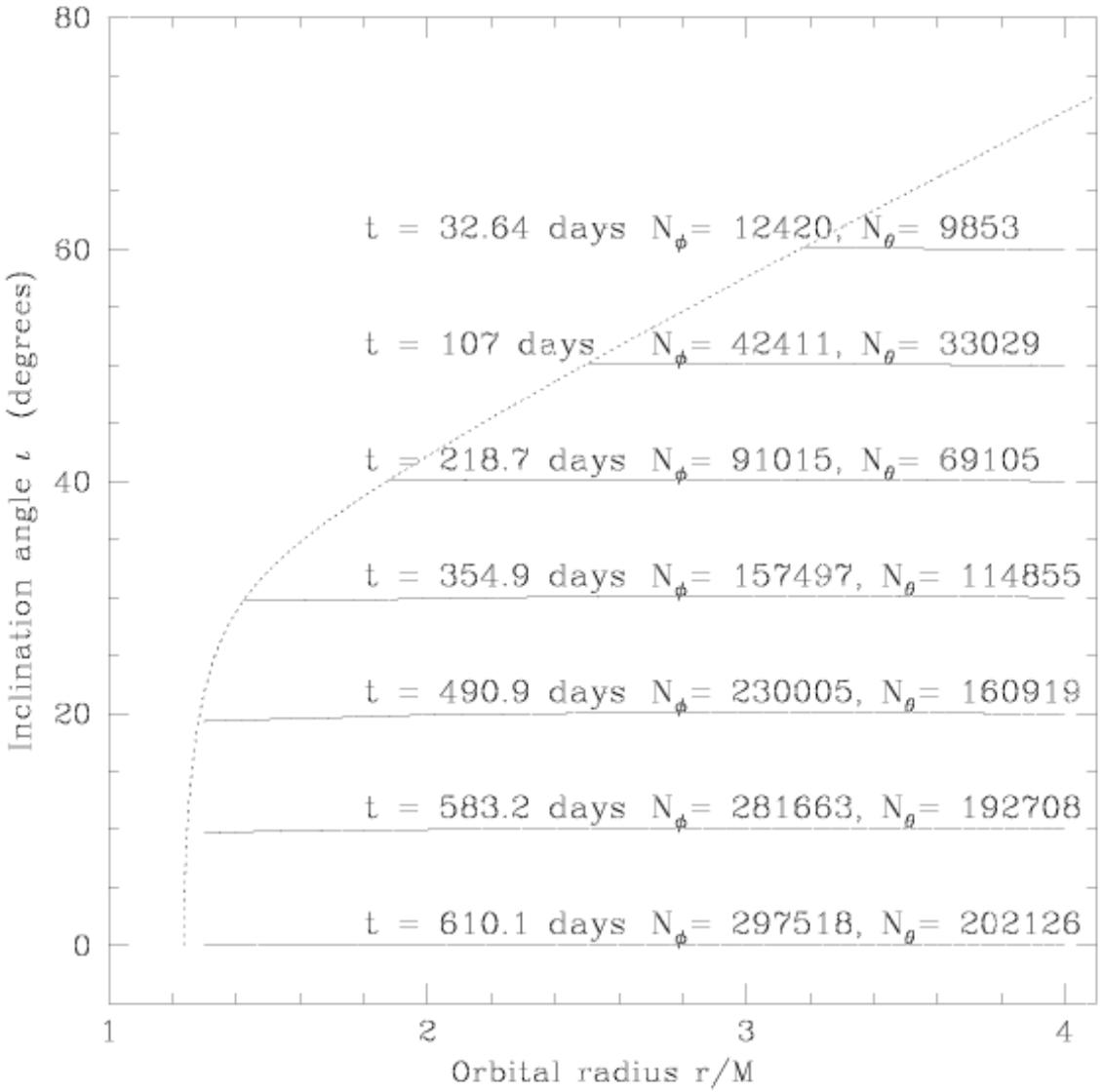

FIG. 3. Inspiral trajectories in the strong field of a Kerr black hole with $a = 0.998M$, ignoring the flux down the horizon — cf. Eq. (2.38), with $\eta = 0$. The figure is otherwise identical to Fig. 2. The trajectory shapes change very slightly (ι does not decrease quite as much over the inspiral), though that effect is very small. Much more interestingly, the inspiral is markedly *faster*: especially at shallow inclination angle, the small body takes several weeks less spiraling to the LSO, and executes many thousands fewer orbits. As discussed in Sec. IV A, this illustrates how tidal coupling between the small body and the event horizon strongly impacts the inspiral: a tidal bulged is raised on the hole, which, due to the hole's rapid rotation in this case, transfers rotational kinetic energy to the small body's orbit.

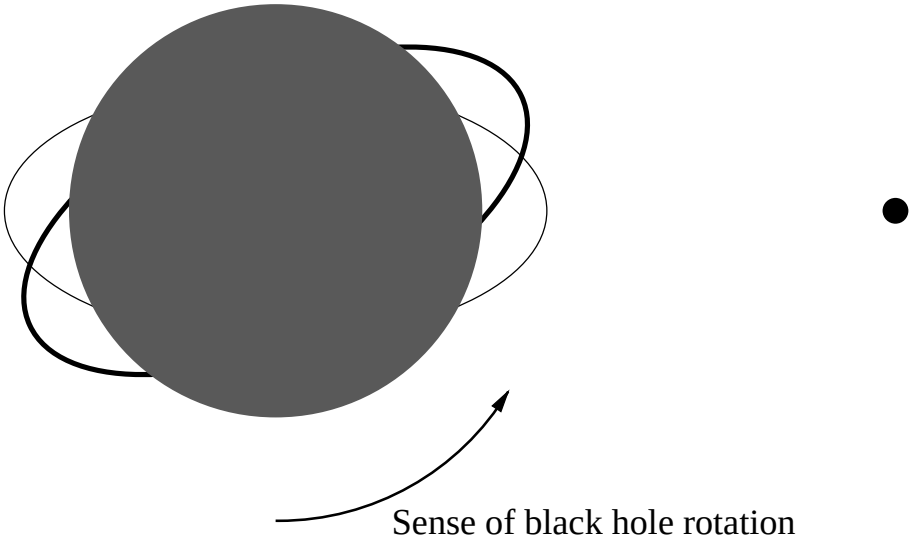

FIG. 4. A cartoon illustrating the tidal bulge raised on the black hole by the orbiting body. This shows the appearance of the event horizon as seen looking down the spin axis in a frame that is co-rotating with the small body's orbit. If the small body were not present, the event horizon's cross section would be circular. The small body raises a tide, distorting the horizon into the shape illustrated by the light ellipse. The hole's rotation then drags that bulge forward, so that the horizon's curvature is most accurately described by the heavy ellipse.

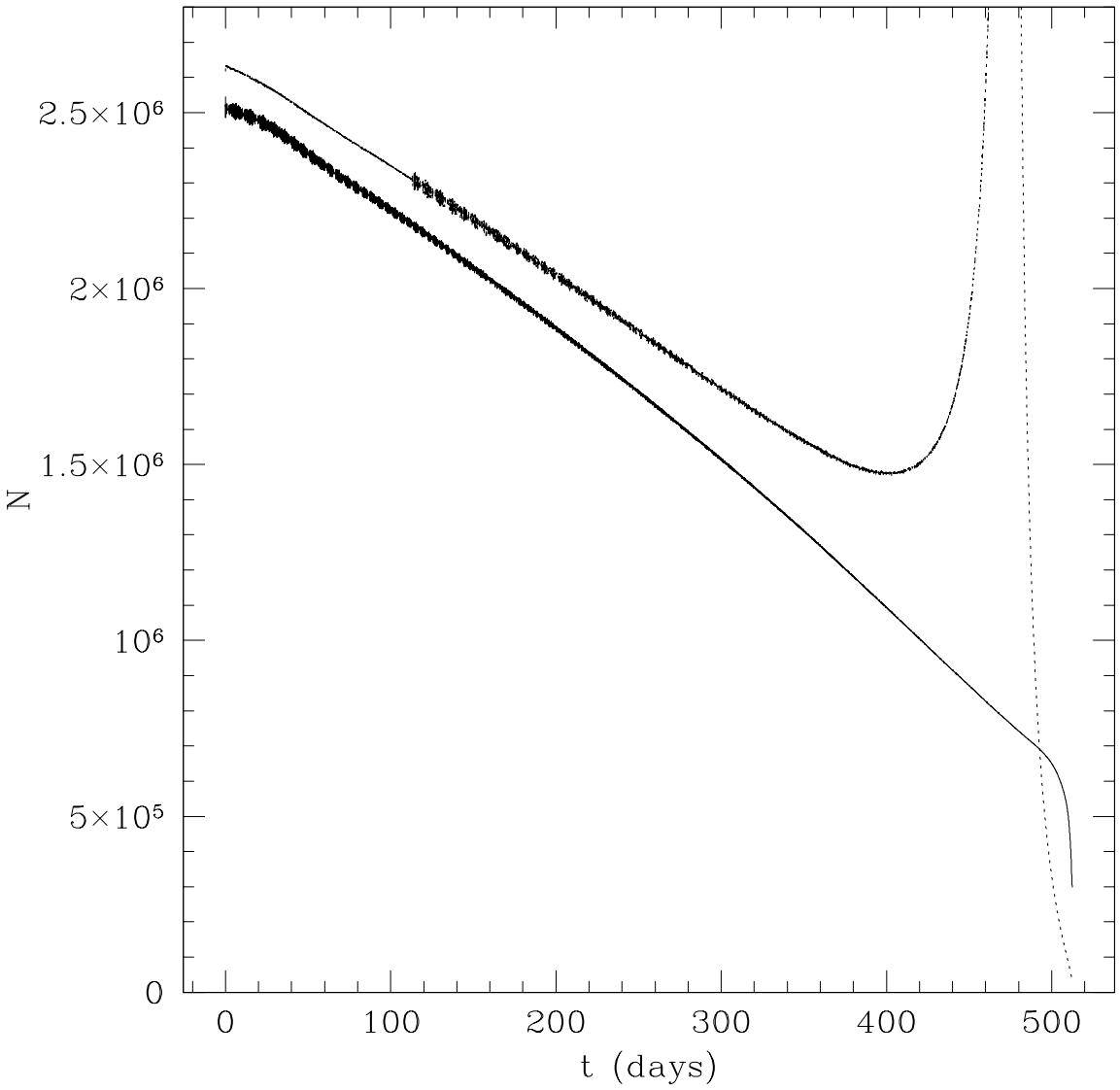

FIG. 5. The evolution of the adiabaticity parameters $\mathcal{N}_{\phi,\theta} = \Omega^2_{\phi,\theta}/2\pi\dot{\Omega}_{\phi,\theta}$ for the inspiral track beginning at $\iota = 20^\circ$ shown in Fig. 2. The solid line is $\mathcal{N}_\phi$, the dotted line $\mathcal{N}_\theta$. Except at the extreme end, $\mathcal{N}_{\phi,\theta} \gg 1$, indicating that the inspiral is indeed adiabatic, as required. Note that $\mathcal{N}_{\phi,\theta} \propto M/\mu$, indicating that the adiabatic requirements are unlikely to be met if $M/\mu < 1000$. The divergence in $\mathcal{N}_\theta$ is due to $\dot{\Omega}_\theta$ passing through zero and changing sign during the inspiral — it ceases chirping up, and begins chirping down.

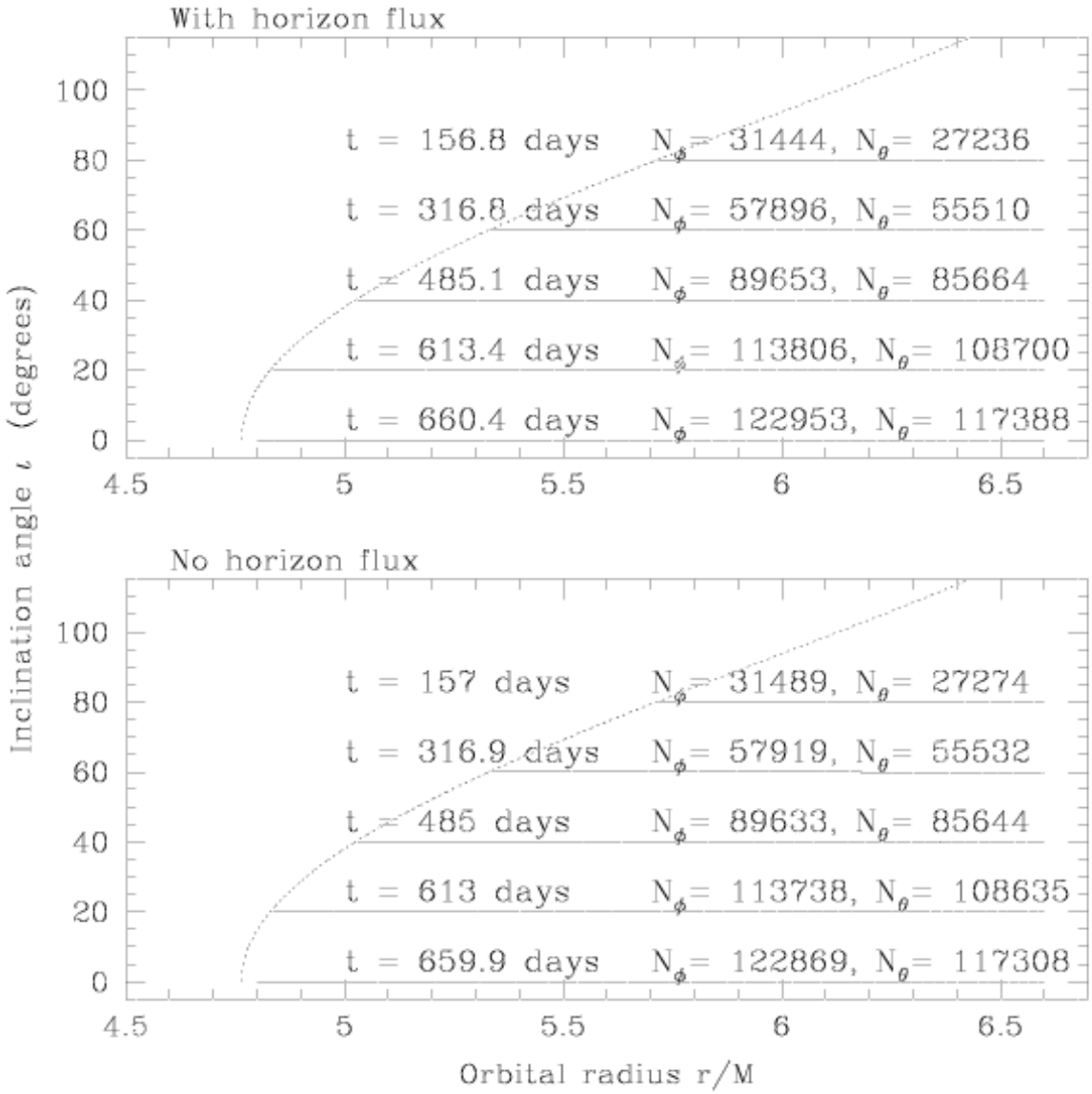

FIG. 6. Inspiral trajectories in the strong field of a Kerr black hole with $a = 0.3594M$. The top panel includes the effects of the down-horizon flux; the bottom panel does not. The span of data is chosen so that the total inspiral duration is similar to that shown in Fig. 2. For this spin, inspiral is nearly identical with the horizon flux included or disincluded: inspiral is slightly faster without horizon flux, but not nearly so much faster as when $a = 0.998M$. This is largely because the spin is not fast enough to drag the tidal bulge on the horizon so far forward. In fact, at the innermost orbits the bulge should be essentially in perfect face-on lock with the orbiting body, since $a = 0.3594M$ is the spin value at which the horizon spin frequency matches the innermost orbital frequency.

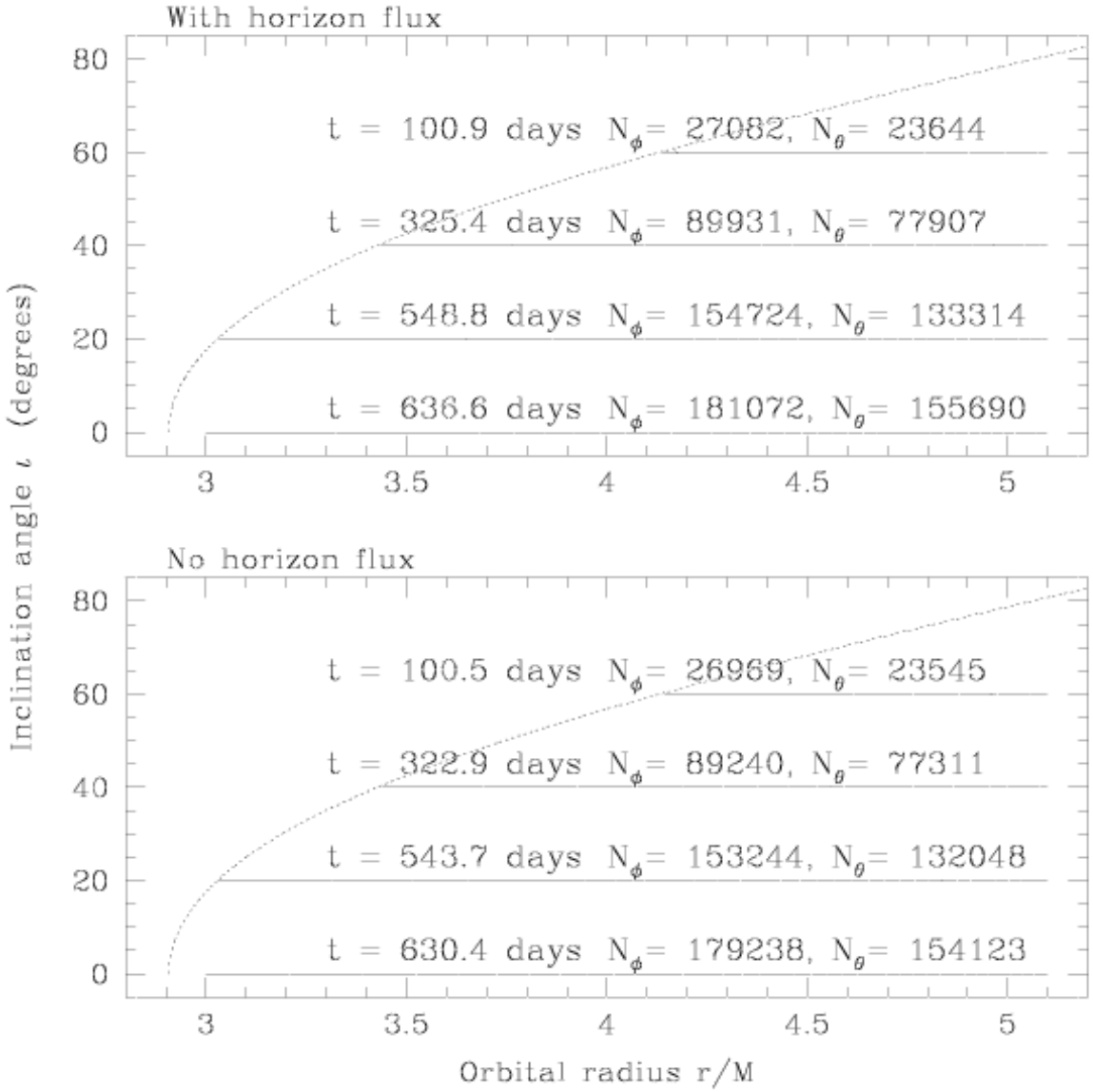

FIG. 7. Inspiral trajectories in the strong field of a Kerr black hole with $a = 0.8M$. The top panel includes the effects of down-horizon flux; the bottom panel does not. The span of data is chosen so that the the total inspiral duration is similar to that shown in Fig. 2. As when $a = 0.998M$, inspiral is quicker when the horizon flux is ignored. However, the magnitude of the effect is much smaller. The torque on the orbit that the horizon's tidal bulge exerts is not as great because the hole rotates less quickly. Also, orbits do not come as close to the horizon for $a = 0.8M$ as they do for $a = 0.998M$.

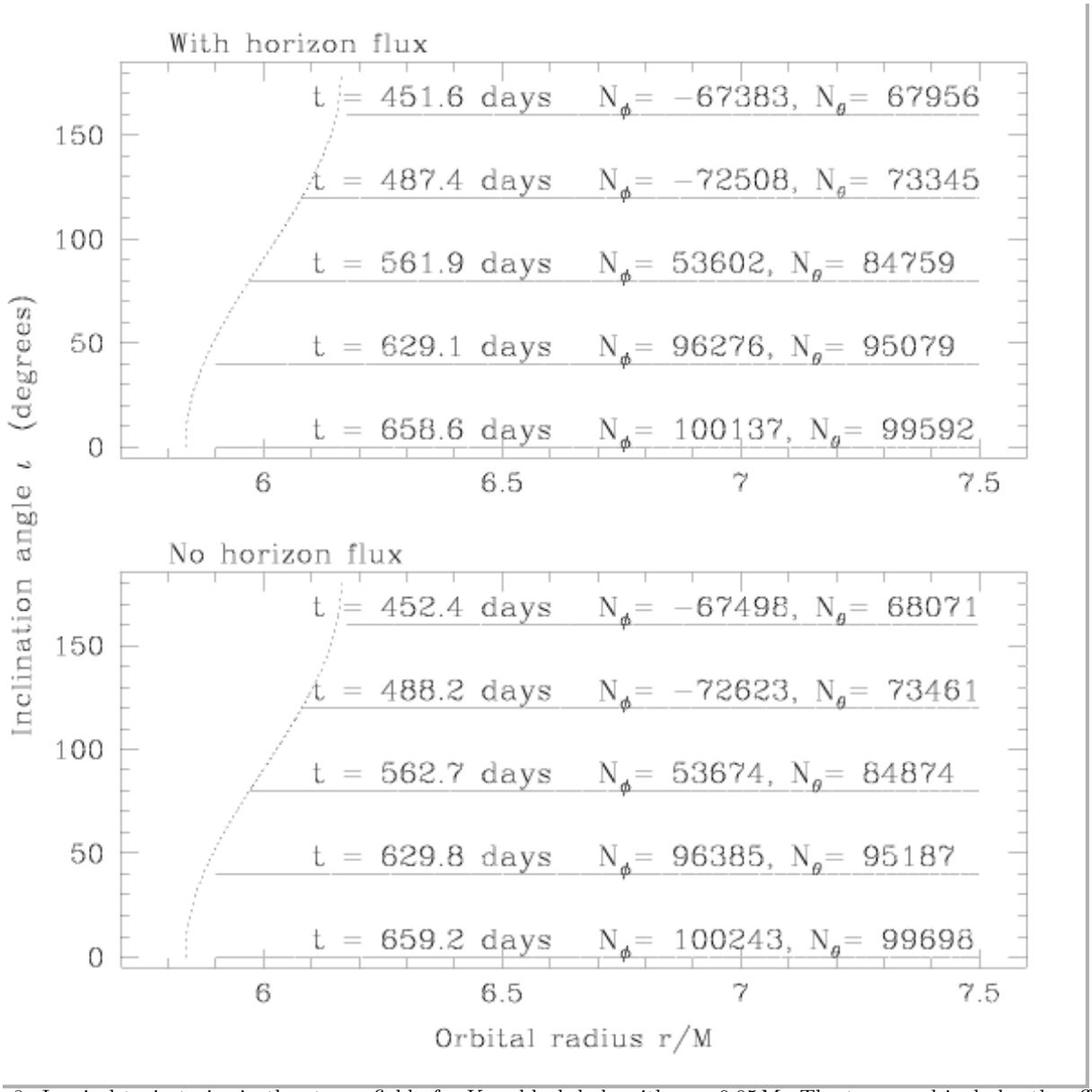

FIG. 8. Inspiral trajectories in the strong field of a Kerr black hole with $a = 0.05M$. The top panel includes the effects of down-horizon flux; the bottom panel does not. In this case, inspiral is quicker when the horizon flux is included: the hole's event horizon acts as an energy sink, as simple intuition suggests it should. This is because the tidal bulge raised on the hole by the orbiting body tends to lag, rather than lead, the orbit. Thus the bulge's torque on the orbit opposes the orbital motion, causing it to spiral in more quickly.

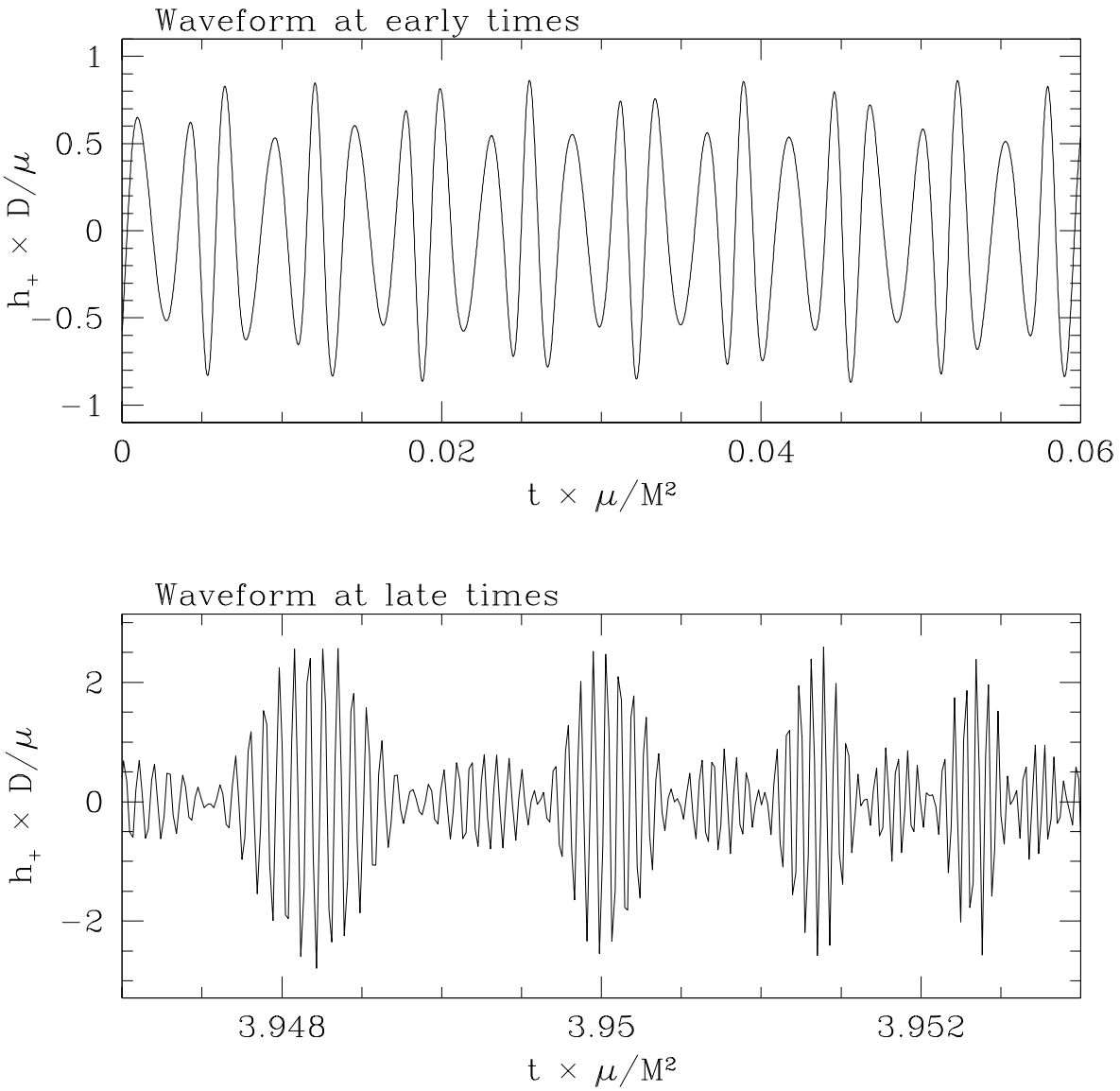

FIG. 9. The + polarization of the gravitational waveform for the inspiral trajectory that begins at $\iota = 40^\circ$ about the $a = 0.998M$ black hole, viewed in the hole's equatorial plane. The upper panel is the waveform at very early times; the lower panel shows the waveform shortly before the inspiraling body plunges into the hole. Notice the very different time scales in the upper and lower panels. This is because of the "chirping" evolution of the frequencies Ω_ϕ and Ω_θ — at late times they are quite a bit larger than they are early on. Many more orbits per unit time are executed late in the inspiral than early.

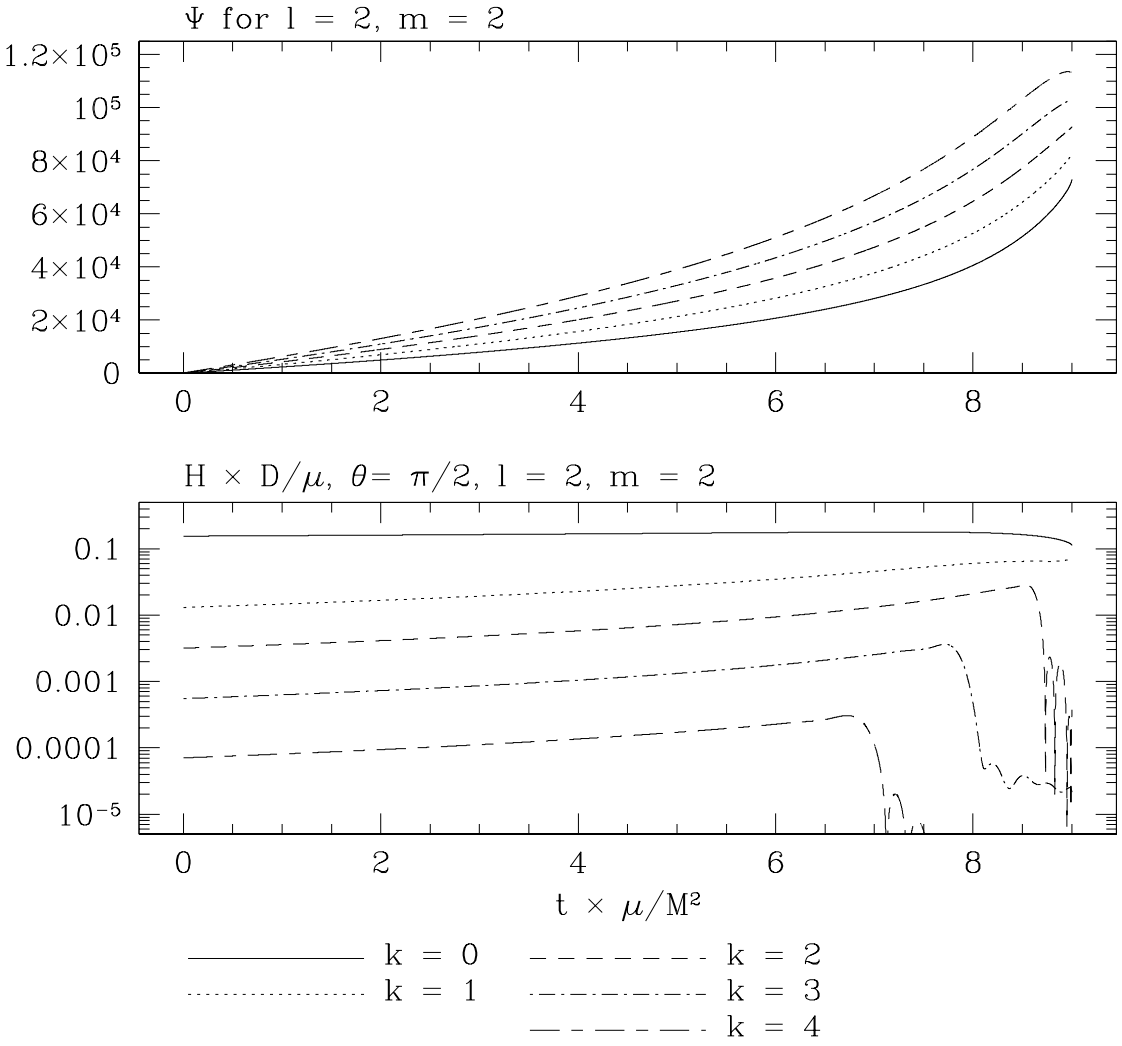

FIG. 10. The phase Ψ_{lmk} and amplitude $\mathcal{H}_{lmk}$ for waveform harmonics $l = 2$, $m = 2$, and k from 0 to 4, and for spiral into a hole with $a = 0.998M$. These amplitudes correspond to measurement in the hole's equatorial plane. Note that harmonics other than $k = 0$ become fairly strong at the end of inspiral. The odd behavior in the amplitude for $k = 2 - 4$ is because of poor computational resolution: the crude parameter space resolution used here was not good enough to accurately capture the change in Z^H_{lmk} at high frequencies as the body spirals in.

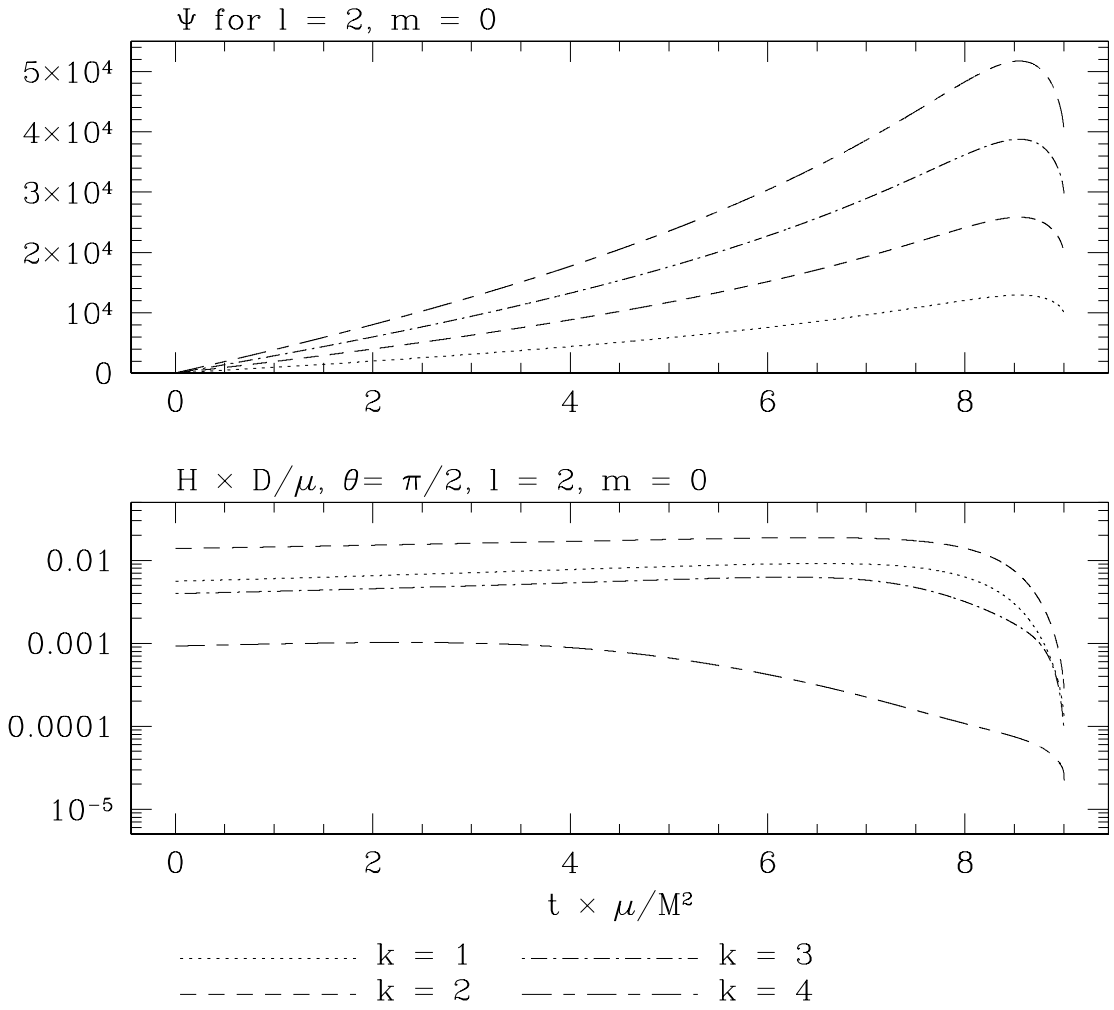

FIG. 11. The phase Ψ_{lmk} and amplitude $\mathcal{H}_{lmk}$ seen in the equatorial plane, for waveform harmonics $l = 2$, $m = 0$, and k from 0 to 4, and for spiral into a hole with $a = 0.998M$. In this case, no frequencies are high enough to cause severe resolution problems, as was the case for $l = 2$, $m = 2$. Note that the phase evolves from high to low late in the inspiral. This is because the phase is dominated by the behavior of Ω_θ, which chirps backwards when the body gets close to the event horizon; cf. Fig. 12. This is essentially a gravitational redshifting effect. Although this is in principle an interesting signature of the black hole's strong field, the wave amplitude gets weak as the frequency gets small. This is not surprising, since the rate of change of the binary's multipole moments decreases with the frequency.

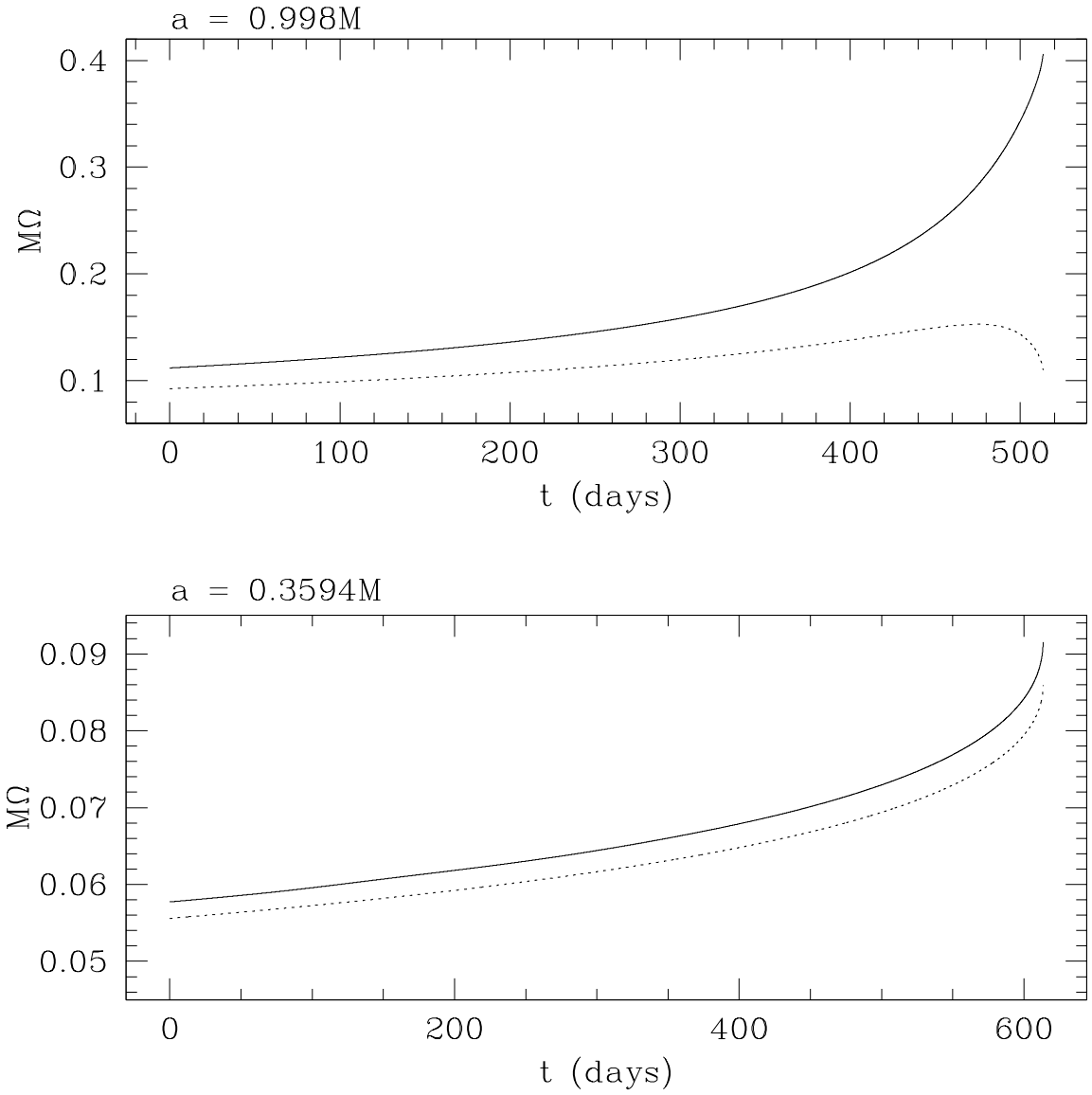

FIG. 12. Evolution of the orbital frequencies Ω_ϕ (solid line) and Ω_θ (dotted line) for inspiral beginning at $\iota = 20°$. The upper panel is for inspiral into a black hole with $a = 0.998M$, the lower for inspiral into a hole with $a = 0.3594M$. In both cases, the behavior of Ω_ϕ is qualitatively "normal": it monotonically chirps upward in a very familiar manner. In the case $a = 0.998M$, the behavior of Ω_θ is comparatively unusual. This is because these orbits are very near to the event horizon — their motion in θ is slowed as seen by distant observers. When $a = 0.3594M$, no orbits come close enough to the horizon for this slowing to have a significant effect. In fact, all orbits in the chosen observation band are at relatively large radius for $a = 0.3594M$, which is why all frequencies are quite smaller than when $a = 0.998M$ (note the different vertical scales in the two panels).

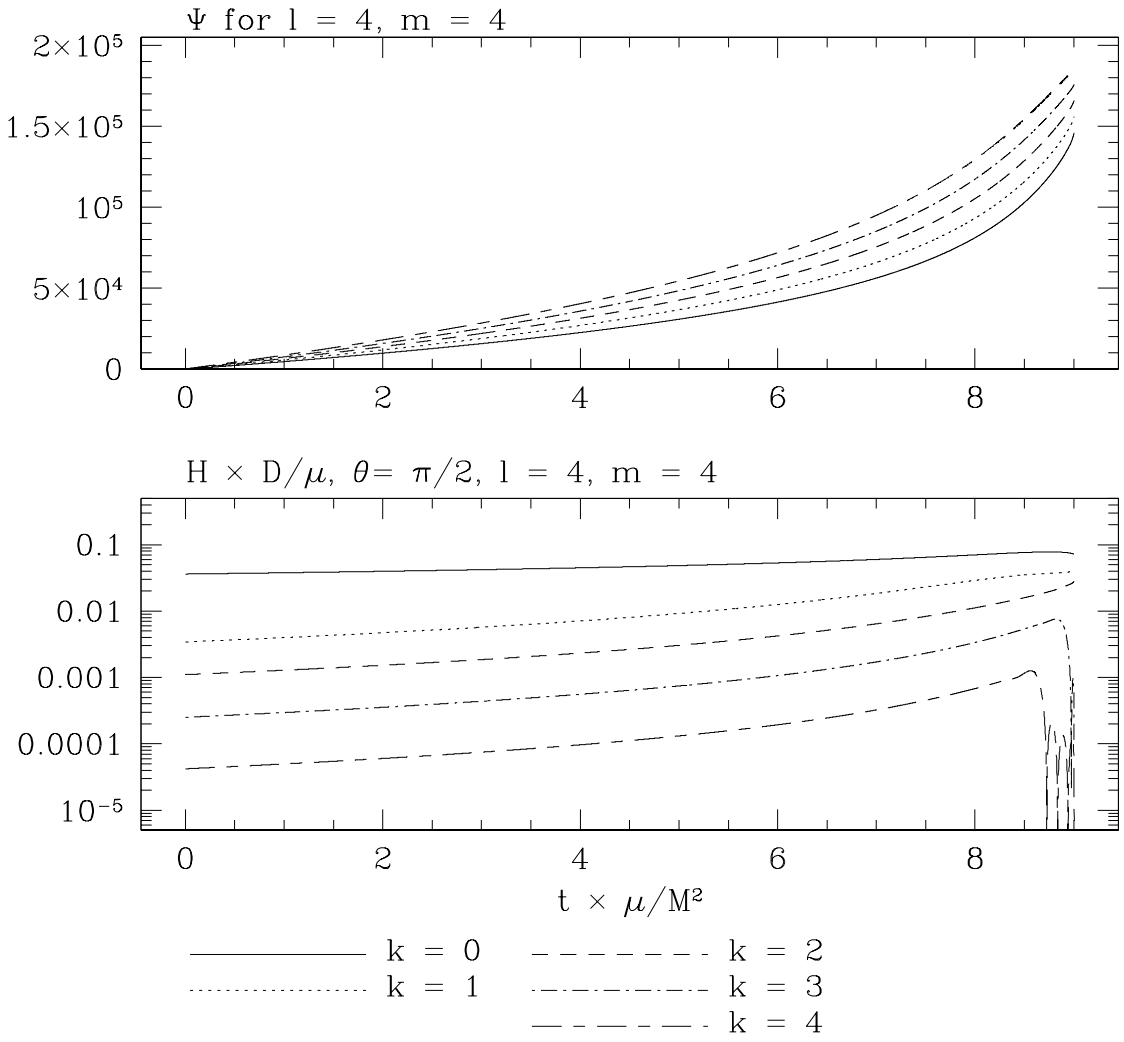

FIG. 13. The phase Ψ_{lmk} and equatorial amplitude $\mathcal{H}_{lmk}$ for waveform harmonics $l = 4$, $m = 4$, and k from 0 to 4, and for spiral into a hole with $a = 0.998M$. The main thing to note in this figure is that the amplitude of the strongest contribution to the waveform is nearly as strong as the dominant $l = 2$, $m = 2$ waves near the end of inspiral. This is a general feature with rapidly rotating holes — radiation at high harmonics of the orbital frequencies tends to be strong. We again see here problems due to poor resolution at for the larger values of k.

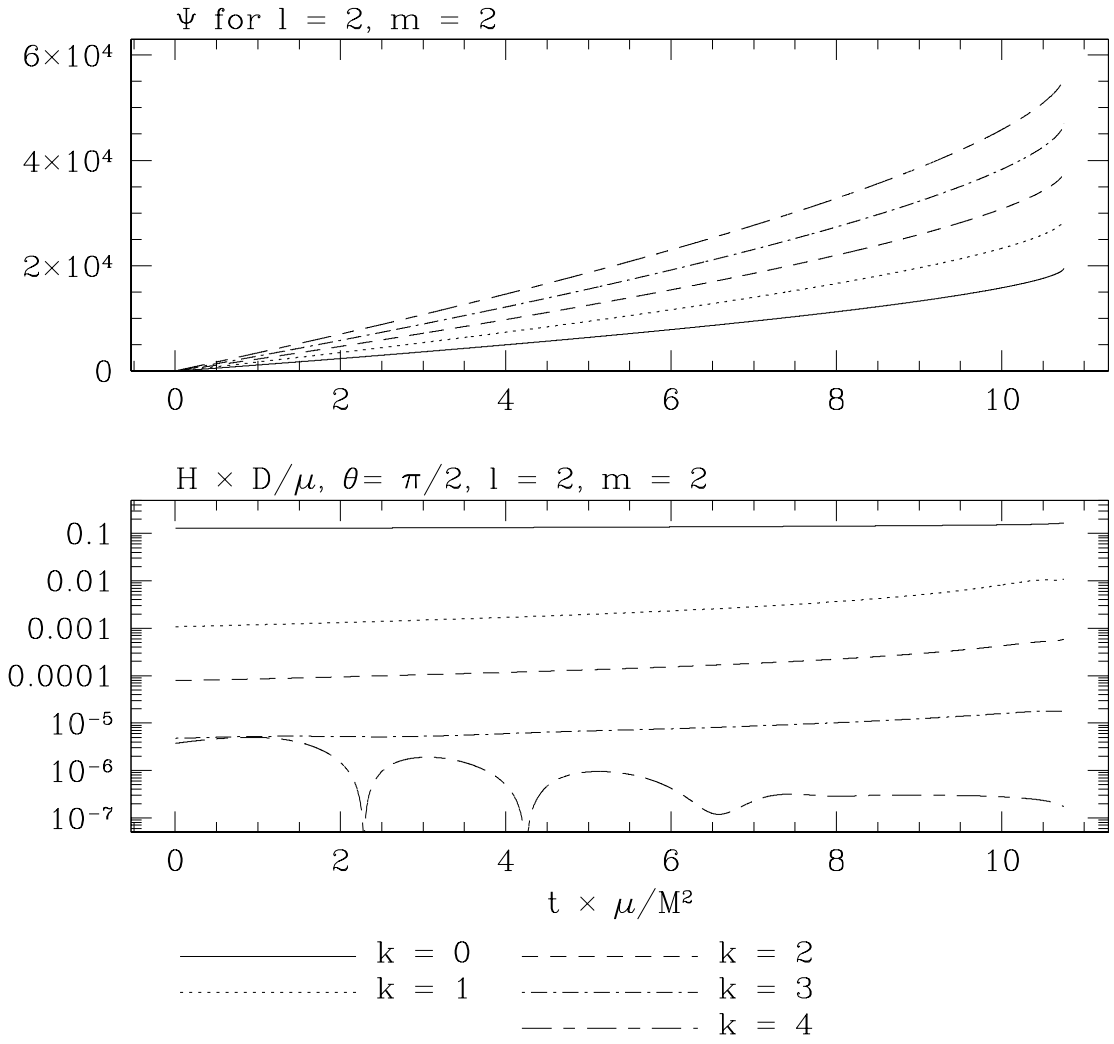

FIG. 14. The phase Ψ_{lmk} and equatorial amplitude $\mathcal{H}_{lmk}$ for waveform harmonics $l = 2$, $m = 2$, and k from 0 to 4, and for spiral into a hole with $a = 0.3494M$. Note that for this spin value, harmonics other than $k = 0$ remain fairly weak all through inspiral — we do not see other voices becoming important, as we do when $a = 0.998M$. Note also that there are no severe resolution problems except at $k = 4$; the frequencies are a fair bit smaller in this case, so the grid spacing turns out to be mostly adequate for all harmonics.

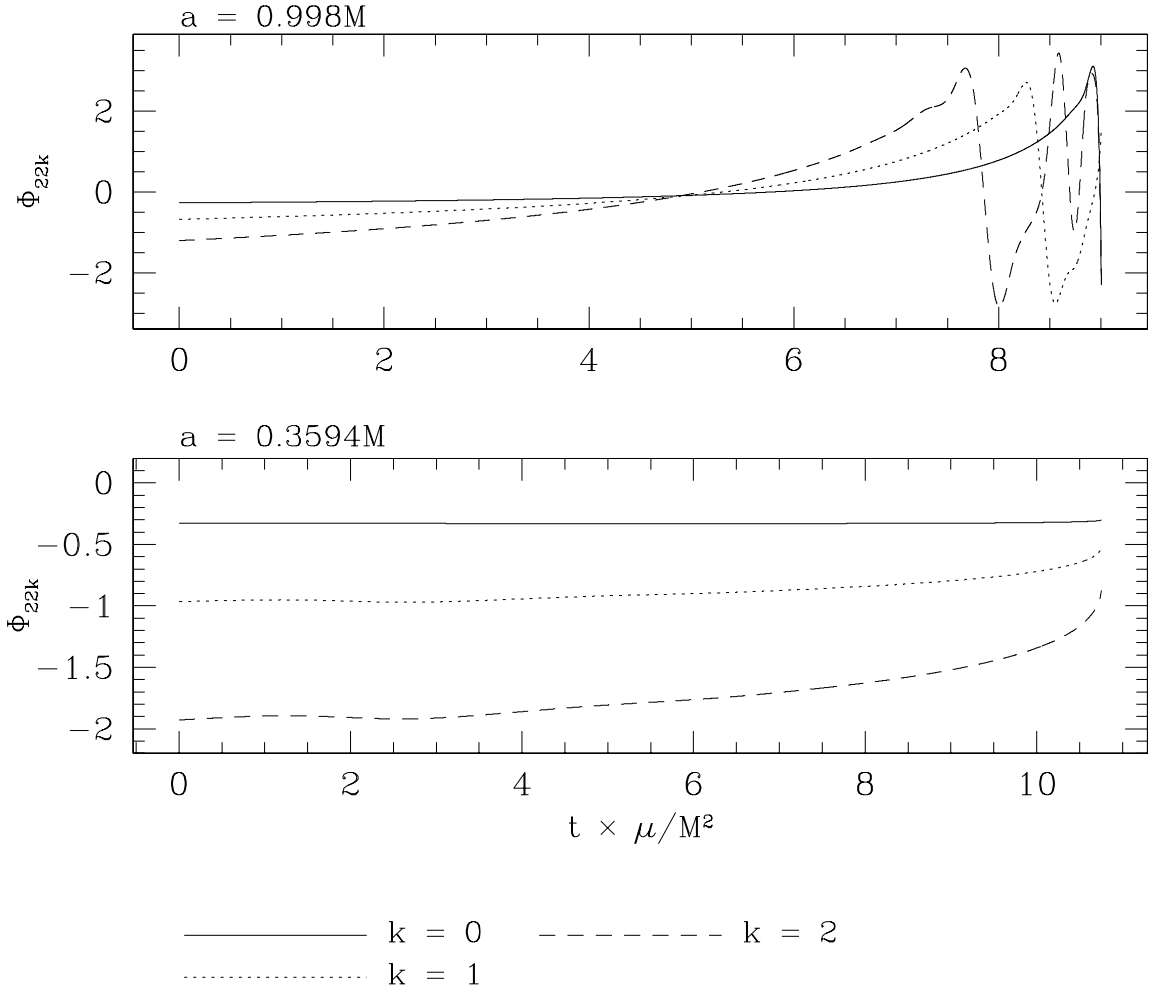

FIG. 15. The phase of the complex coefficient Z^H_{lmk} for $l = 2$, $m = 2$ and k from 0 to 2. This phase contributes to the overall phase Ψ_{lmk} for each harmonic voice. The top panel is for $a = 0.998M$. The jumpiness towards the end of inspiral is because of poor resolution, and because the numerical arctangent function tends to put all phases between $-\pi$ and π; this behavior could easily be fixed with better resolution and adding or subtracting 2π to keep the phases's behavior monotonic. The lower panel is for $a = 0.3594M$. All tracks are nicely smooth in this case. Note that the change in all phases is very small relative to the total phase accumulated during an inspiral, $\sim 10^5 - 10^7$ radians.